SANDIA REPORT

SAND2016-0804
Unlimited Release
Printed January 29, 2016

Verification and Validation of a Coordinate-Transformation Method in Axisymmetric Transient Magnetics

C. Chace Ashcraft, John H. J. Niederhaus and Allen C. Robinson

Prepared by
Sandia National Laboratories
Albuquerque, New Mexico 87185 and Livermore, California 94550

Sandia National Laboratories is a multi-program laboratory managed and operated by Sandia Corporation, a wholly owned subsidiary of Lockheed Martin Corporation, for the U.S. Department of Energy's National Nuclear Security Administration under contract DE-AC04-94AL85000.

Sandia National Laboratories

Issued by Sandia National Laboratories, operated for the United States Department of Energy by Sandia Corporation.

Available to DOE and DOE contractors from
U.S. Department of Energy
Office of Scientific and Technical Information
P.O. Box 62
Oak Ridge, TN 37831

Telephone: (865) 576-8401
Facsimile: (865) 576-5728
E-Mail: reports@adonis.osti.gov
Online ordering: http://www.osti.gov/bridge

Available to the public from
U.S. Department of Commerce
National Technical Information Service
5285 Port Royal Rd
Springfield, VA 22161

Telephone: (800) 553-6847
Facsimile: (703) 605-6900
E-Mail: orders@ntis.fedworld.gov
Online ordering: http://www.ntis.gov/help/ordermethods.asp?loc=7-4-0#online

SAND2016-0804
Unlimited Release
Printed January 29, 2016

Verification and Validation of a Coordinate-Transformation Method in Axisymmetric Transient Magnetics

C. Chace Ashcraft, John H. J. Niederhaus and Allen C. Robinson
Computational Shock and Multiphysics
Sandia National Laboratories
P.O. Box 5800, MS-1323
Albuquerque, NM 87185-1323
acrobin@sandia.gov

Abstract

We present a verification and validation analysis of a coordinate-transformation-based numerical solution method for the two-dimensional axisymmetric magnetic diffusion equation, implemented in the finite-element simulation code ALEGRA. The transformation, suggested by Melissen and Simkin, yields an equation set perfectly suited for linear finite elements and for problems with large jumps in material conductivity near the axis. The verification analysis examines transient magnetic diffusion in a rod or wire in a very low conductivity background by first deriving an approximate analytic solution using perturbation theory. This approach for generating a reference solution is shown to be not fully satisfactory. A specialized approach for manufacturing an exact solution is then used to demonstrate second-order convergence under spatial refinement and temporal refinement. For this new implementation, a significant improvement relative to previously available formulations is observed. Benefits in accuracy for computed current density and Joule heating are also demonstrated. The validation analysis examines the circuit-driven explosion of a copper wire using resistive magnetohydrodynamics modeling, in comparison to experimental tests. The new implementation matches the accuracy of the existing formulation, with both formulations capturing the experimental burst time and action to within approximately 2%.

Acknowledgment

This work was jointly supported by the U.S. Army Research Laboratory and the U.S. Department of Energy's National Nuclear Security Administration.

Contents

List of Figures

Chapter 1

Introduction

The ALEGRA code solves the resistive magnetohydrodynamic (MHD) equations in an arbitrary Lagrangian-Eulerian (ALE) computational framework [6]. These continuum equations are used to model high-current, high-energy field phenomena in conducting media. Operator splitting in time in ALEGRA results in a transient magnetic sub-problem of the form:

$$\frac{\partial \mathbf{B}}{\partial t} = -\nabla \times (\frac{1}{\sigma}(\nabla \times \frac{\mathbf{B}}{\mu})) \tag{1.1}$$

or, in vector potential form,

$$\sigma \left(-\frac{\partial \mathbf{A}}{\partial t} - \nabla \phi \right) = \nabla \times (\frac{\nabla \times \mathbf{A}}{\mu}). \tag{1.2}$$

where σ is the material conductivity of the continuum, μ is the magnetic permeability of the continuum, $\mathbf{B}$ is the magnetic flux density, $\mathbf{A}$ is the vector potential and ϕ is the scalar potential.

In this report, we are interested in the two dimensional simplifications of these equations when the problem is axisymmetric and the only dependent variable is the out-of-plane magnetic flux density component, B_θ.

Code has already been developed in ALEGRA to solve for B_θ under these conditions with the constraint that the magnetic permeability, μ, is constant. We seek to improve the B_θ code as currently implemented. We show that for a specially chosen test problem, one of the original formulations of the code, which is referred to as the FIFE (Fully Integrated Finite Element) formulation, can converge very slowly to the correct solution. An alternate formulation, which is called the R-Scaled formulation, solves for rB_θ and converges much more rapidly, but it tends to be inaccurate near $r = 0$, where r is the radial coordinate in a cylindrically symmetric coordinate system. Both of these issues restrict the analyst's ability to resolve problems of interest, so here we implement a new formulation, referred to as the PSI-S formulation, to rectify these issues.

The PSI-S formulation is inspired by a paper written by J.B.M. Melissen and J. Simkin [10]. In their paper, they apply a clever change of radial coordinates to the axisymmetric version of Equation 1.2 when using the out-of-plane vector potential times r as the dependent scalar field. This resulted in a large overall improvement in the discrete error. They show excellent improvement in

accuracy for material property jumps in μ near the axis. We use the same strategy with Equation 1.1 to produce the PSI-S formulation and expect much improved results for problems with conductivity jumps near the axis. We will see that the analytic modification to the equations generates an equation set perfectly suited for linear finite elements.

Thus, we expect the PSI-S formulation to be more accurate and to converge faster than the current formulations, and in order to demonstrate this superiority, we perform a verification analysis and report the results below.

We also examine some consequences of the PSI-S formulation beyond verification of the fundamental field variable. Several variables show improved computational accuracy with the PSI-S formulation. Further study is required to completely understand the effects of the PSI-S formulation on these variables, but some results are immediately apparent and these are the ones we show. In addition, we use the PSI-S formulation on an exploding wire simulation to see how it performs on a much larger and more complicated problem, and then compare its performance to the R-Scaled formulation. The results are significant enough for us to recommend future study on the differences between the two formulations and suggest that a validation study would be particularly useful.

As a final note, if a non-constant μ is necessary or desirable, we stress that one would need to modify the B_θ formulation slightly to solve using an H_θ nodal finite element approach in order to satisfy continuity requirements on H. In addition, in the case of in-plane fields with variable μ, the A_θ formulation in ALEGRA is applicable and the approach discussed in this report would apply and would provide improved fidelity for non-constant μ. These possible developments are under consideration but are not covered in this report.

Chapter 2

Finite Element Formulations

Under 2D cylindrically symmetric assumptions, ALEGRA performs computations in an (r,z) coordinate system, where r represents the radius in cylindrical geometry, and z represents the orthogonal direction in the plane. Following Melissen and Simkin, we perform a coordinate change on the R-Scaled formulation, taking it from (r,z) coordinates to (s,z) coordinates, where $s = r^2$ and setting $\psi = rB_\theta$ to be the dependent variable. This relatively simple change moves the radial axis singularity in the magnetic diffusion equations from its position in the radial spatial operator to a benign position in the mass matrix and the z differential operator. This transformation is the foundation of our entire report. In this chapter we write down the magnetic diffusion equations and their finite element matrix equivalents for the different formulations and show how they differ. The FIFE and R-Scaled formulations are described in a broader ALEGRA context in [8]. We restate and clarify these equations below and then offer here a complete and detailed derivation of the PSI-S formulation.

Magnetic Diffusion Equations

We begin with the magnetic diffusion equation that ALEGRA solves after the Lagrangian hydrodynamic motion step. This is Equation 1.1 written in cylindrically symmetric coordinates and assuming only out-of-plane magnetic field components in the azimuthal direction. In general, the permeability, μ, cannot be brought out from the innermost partial derivative of the right-hand-side since, in general, it may be a function of location and material state. However, for the purposes of this formulation, it is required to be constant and is thus written together with the resistivity, $\eta = 1/\sigma$. For the purposes of this report the flux density, B_θ, and the magnetic field, H_θ are proportional, $B_\theta = \mu H_\theta$, and $\mu = \mu_0$ is the constant permeability of free space.

The resulting scalar equation in 2D *cylindrical* geometry for B_θ is

$$\frac{\partial B_\theta}{\partial t} = \frac{\partial}{\partial r}\left(\frac{\eta}{\mu r}\frac{\partial (rB_\theta)}{\partial r}\right) + \frac{\partial}{\partial z}\left(\frac{\eta}{\mu}\frac{\partial B_\theta}{\partial z}\right) \tag{2.1}$$

Multiplying Equation 2.1 by r, we obtain an equation for the magnetic stream function, $\psi = rB_\theta$,

$$\frac{\partial \psi}{\partial t} = r\frac{\partial}{\partial r}\left(\frac{\eta}{\mu r}\frac{\partial \psi}{\partial r}\right) + \frac{\partial}{\partial z}\left(\frac{\eta}{\mu}\frac{\partial \psi}{\partial z}\right). \tag{2.2}$$

Alternatively, by dividing Equation 2.1 by $2r$, and making the Melissen-Simkin change of coordinates: $s = r^2$, with $ds = 2rdr$, we obtain an alternate magnetic diffusion equation for the stream function,

$$\frac{1}{2s}\frac{\partial \psi}{\partial t} = \frac{\partial}{\partial s}\left(\frac{2\eta}{\mu}\frac{\partial \psi}{\partial s}\right) + \frac{\partial}{\partial z}\left(\frac{\eta}{2s\mu}\frac{\partial \psi}{\partial z}\right). \tag{2.3}$$

Note that s does not appear inside an s derivative, showing that we have removed the radial coordinate from inside the radial spatial operator. The factor of $1/2$ arises from the desire to ensure a consistent energy definition across the weak forms discussed below.

Discrete Magnetic Diffusion Equations

We now summarize the finite element weak form equations for the magnetic diffusion operator for the three formulations below. This is accomplished by multiplying each equation by a test function, integrating over the volume and utilizing the divergence theorem to reduce the order of derivatives. The equations are written in such a form that replacing the test function by the solution gives a magnetic energy equation with an equivalent magnetic energy definition between the three equations. The required additional factor of 2π is not shown however.

The weak form for the FIFE formulation ($B_\theta(r,z,t)$) is

$$\int_{\Omega_e} W\frac{\partial B_\theta}{\partial t} rdrdz + \int_{\Omega_e}\left(\left(\frac{1}{r}\frac{\partial (rW)}{\partial r}\right)\frac{\eta}{\mu}\left(\frac{1}{r}\frac{\partial (rB_\theta)}{\partial r}\right) + \frac{\partial W}{\partial z}\frac{\eta}{\mu}\frac{\partial B_\theta}{\partial z}\right) rdrdz = \int_{\Gamma_e} rW\mathbf{E}\cdot\mathbf{t}dl \tag{2.4}$$

where by Ohm's Law, $\mathbf{E} = \eta\mathbf{J}$, is the electric field in the plane, $\mathbf{t}$ is the unit tangent vector, and l is arc-length in the (r,z) plane. The discrete magnetic flux density, B_θ, is assumed to vary bi-linearly within each quadrilateral mesh element in a piece-linear function space with a basis set given by the finite element hat functions, N_j. The test functions W_i are from the same discrete space. Therefore, we have the represention $B_\theta = \sum_j B_j N_j$ and applying all possible test functions leads to a global equation set. ALEGRA assumes a backward Euler time discretization and integrates the Neumann boundary condition term via a midpoint quadrature in time. Continuity of tangential electric field provides for cancelling Neumann terms at interior element boundaries and thus does not need to be computed there. Thus,

$$\frac{1}{\Delta t} M_{ij} \left(B_j^{n+1} - B_j^n \right) + K_{ij} B_j^{n+1} = L_i^{n+1/2} \tag{2.5}$$

where

$$\begin{aligned} M_{ij} &= \sum_{e \in i} \int_{\Omega_e} N_i N_j r dr dz \\ K_{ij} &= \sum_{e \in i} \int_{\Omega_e} \left(\left(\frac{\partial N_i}{\partial r} + \frac{N_i}{r} \right) \frac{\eta}{\mu} \left(\frac{\partial N_j}{\partial r} + \frac{N_i}{r} \right) + \frac{\partial N_i}{\partial z} \frac{\eta}{\mu} \frac{\partial N_j}{\partial z} \right) r dr dz \\ L_i^{n+1/2} &= \sum_{e \in i} \int_{\Gamma_e} r N_i \mathbf{E}^{n+1/2} \cdot \mathbf{t} dl. \end{aligned} \tag{2.6}$$

The weak form for the R-Scaled formulation ($\psi(r,z)$) is

$$\begin{aligned} \int_{\Omega_e} W \frac{1}{r} \frac{\partial \psi}{\partial t} dr dz + \int_{\Omega_e} \left(\frac{\partial W}{\partial r} \frac{\eta}{r\mu} \frac{\partial \psi}{\partial r} + \frac{\partial W}{\partial z} \frac{\eta}{r\mu} \frac{\partial \psi}{\partial z} \right) dr dz \\ = \int_{\Gamma_e} W \mathbf{E} \cdot \mathbf{t} dl \end{aligned} \tag{2.7}$$

where $\mathbf{E}$, $\mathbf{t}$, and l are same as in the FIFE weak form. We again have $\psi = \sum_j \psi_j N_j$ and the global equation

$$\frac{1}{\Delta t} M_{ij} \left(\psi_j^{n+1} - \psi_j^n \right) + K_{ij} \psi_j^{n+1} = L_i^{n+1/2} \tag{2.8}$$

where

$$\begin{aligned} M_{ij} &= \sum_{e \in i} \int_{\Omega_e} N_i \frac{1}{r} N_j dr dz \\ K_{ij} &= \sum_{e \in i} \int_{\Omega_e} \left(\frac{\partial N_i}{\partial r} \frac{\eta}{r\mu} \frac{\partial N_j}{\partial r} + \frac{\partial N_i}{\partial z} \frac{\eta}{r\mu} \frac{\partial N_j}{\partial z} \right) dr dz \\ L_i^{n+1/2} &= \sum_{e \in i} \int_{\Gamma_e} N_i \mathbf{E}^{n+1/2} \cdot \mathbf{t} dl. \end{aligned} \tag{2.9}$$

We now derive the weak form for the PSI-S formulation ($\psi(s,z,t)$). Beginning with Equation 2.3, we multiply by an arbitrary test function W and take a scaled volume integral of 2.3 on an arbitrary element e, resulting in Equation 2.10 where Ω_e represents the domain of element e. The

factor of $1/2$ ensures that the quadratic form associated with the magnetic energy is scaled to match the weak forms of the other formulations.

$$\begin{aligned}\int_{\Omega_e} W\frac{1}{2s}\frac{\partial\psi}{\partial t}dsdz &= \int_{\Omega_e} W\left(\frac{\partial}{\partial s}\left(\frac{2\eta}{\mu}\frac{\partial\psi}{\partial s}\right)+\frac{\partial}{\partial z}\left(\frac{\eta}{2s\mu}\frac{\partial\psi}{\partial z}\right)\right)dsdz \\ &= \int_{\Omega_e} W\left(\nabla\cdot M(s)\nabla\psi\right)dzdz \end{aligned} \tag{2.10}$$

where

$$M(s) = \begin{bmatrix} \frac{2\eta}{\mu} & 0 \\ 0 & \frac{\eta}{2\mu s} \end{bmatrix}.$$

Since W is a scalar quantity, we can use the vector calculus identity

$$\nabla\cdot(f\mathbf{A}) = (\nabla f)\cdot\mathbf{A} + f\left(\nabla\cdot\mathbf{A}\right) \tag{2.11}$$

where f is a scalar function and $\mathbf{A}$ is a vector function in the form

$$\nabla\cdot(WM\nabla\psi) = \nabla W\cdot(M\nabla\psi) + W\left(\nabla\cdot M\nabla\psi\right)$$

to obtain

$$\int_{\Omega_e} W\frac{1}{2s}\frac{\partial\psi}{\partial t}dsdz = \int_{\Omega_e}\nabla\cdot(WM\nabla\psi)\,dsdz - \int_{\Omega_e}\nabla W\cdot(M\nabla\psi)\,dsdz. \tag{2.12}$$

Applying the divergence theorem,

$$\int_{\Omega}(\nabla\cdot\mathbf{F})\,dV = \int_{\partial\Omega}(\mathbf{F}\cdot\mathbf{n})\,dS \tag{2.13}$$

to Equation 2.12, gives

$$\int_{\Omega_e} W\frac{1}{2s}\frac{\partial\psi}{\partial t}dsdz + \int_{\Omega_e}\nabla W\cdot(M\nabla\psi)\,dsdz = \int_{\Gamma_e}(WM\nabla\psi)\cdot\mathbf{n}dl \tag{2.14}$$

where $\mathbf{n}$ is the unit vector in the plane normal to the boundary and Γ_e denotes the boundary of the element e. Therefore,

$$\int_{\Omega_e} W \frac{1}{2s} \frac{\partial \psi}{\partial t} ds dz + \int_{\Omega_e} \nabla W \cdot (M \nabla \psi) \, ds dz = \int_{\Gamma_e} (W M \nabla \psi) \cdot \mathbf{n} dl. \tag{2.15}$$

Using Ohm's law, Equation 2.15 further simplifies to

$$\begin{aligned} \int_{\Omega_e} W \frac{1}{2s} \frac{\partial \psi}{\partial t} ds dz + \int_{\Omega_e} \nabla W \cdot (M \nabla \psi) \, ds dz &= \int_{\Gamma_e} W (S \eta \mathbf{J}) \cdot \mathbf{t} dl \\ &= \int_{\Gamma_e} W (S \mathbf{E}) \cdot \mathbf{t} dl \end{aligned} \tag{2.16}$$

where

$$\mathbf{J} = -\frac{1}{\mu \sqrt{s}} \frac{\partial \psi}{\partial z} \hat{s} + \frac{2}{\mu} \frac{\partial \psi}{\partial s} \hat{z} \tag{2.17}$$

is the current density in the plane, $\mathbf{t} = (-\mathbf{n}_z, \mathbf{n}_s)$ is the unit tangent vector, $\mathbf{E} = \eta \mathbf{J}$ is the electric field, and

$$S = \begin{bmatrix} \frac{1}{2\sqrt{s}} & 0 \\ 0 & 1 \end{bmatrix}. \tag{2.18}$$

Finally

$$\int_{\Omega_e} W \frac{1}{2s} \frac{\partial \psi}{\partial t} ds dz + \int_{\Omega_e} \left(\frac{\partial W}{\partial s} \frac{2\eta}{\mu} \frac{\partial \psi}{\partial s} + \frac{\partial W}{\partial z} \frac{\eta}{2\mu s} \frac{\partial \psi}{\partial z} \right) ds dz = \int_{\Gamma_e} W (S \mathbf{E}) \cdot \mathbf{t} dl \tag{2.19}$$

Again assuming linear finite element shape functions and $\psi = \sum_j \psi_j N_j$ we obtain the following global equation:

$$\frac{1}{\Delta t} M_{ij} \left(\psi_j^{n+1} - \psi_j^n \right) + K_{ij} \psi_j^{n+1} = L_i^{n+1/2} \tag{2.20}$$

with elemental matrices

$$
\begin{aligned}
M_{ij} &= \sum_{e \in i} \int_{\Omega_e} N_i \frac{1}{2s} N_j \, ds dz \\
K_{ij} &= \sum_{e \in i} \int_{\Omega_e} \left(\frac{\partial N_i}{\partial s} \frac{2\eta}{\mu} \frac{\partial N_j}{\partial s} + \frac{\partial N_i}{\partial z} \frac{\eta}{2\mu s} \frac{\partial N_j}{\partial z} \right) ds dz \\
L_i^{n+1/2} &= \sum_{e \in i} \int_{\Gamma_e} N_i \left(S \mathbf{E}^{n+1/2} \right) \cdot \mathbf{t} \, dl.
\end{aligned}
\tag{2.21}
$$

Note the presence of the $1/s$ terms appearing in the integrals in Equation 2.19. While these terms might initially appear to be problematic as $s \to 0$, zero Dirichlet conditions are imposed on the solution on the axis and the solution and the test functions are $O(s)$ as $s \to 0$. Examination of the weak form shows that no singular integrals are required to be calculated.

Chapter 3

A Relevant Verification Problem

In order to perform our verification analysis, we need to design a test problem that is simple enough for analytic study, yet has all the features of a typical MHD problems of interest so that we can be sure to stress the numerical algorithm in a relevant way. We are interested in problems which have large jumps in material conductivity near the axis.

Our problem of choice is a wire in a void model, with a constant, axial-tangential electric field assumed to exist instantaneously along the interface at time $t = 0$. Figure 3.1 shows the problem's physical set up: A cylindrical rod of height h, radius a, and conductivity σ_r, surrounded by a void region of conductivity $\sigma_v \ll \sigma_r$, and radial depth $b - a$. Because the B_θ formulation requires a constant magnetic permeability μ, we set $\mu = \mu_0$, the magnetic permeability of free space, everywhere. We assume an instantaneous jump at $t = 0$ to a constant, axial-tangential electric field along the interface of the rod and the void, which generates a time dependent magnetic flux, B_θ, through the rod and the void.

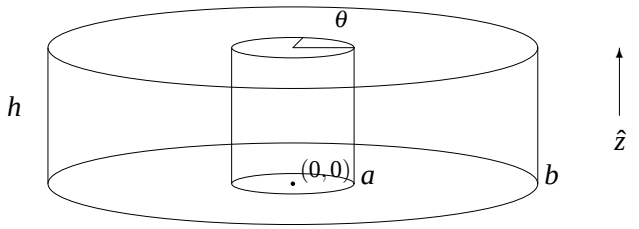

Figure 3.1: Metal Rod in a Void

Inside the rod, the solution for B_θ should appear as a magnetic diffusion wave into the rod early in time until reaching a radial linear steady state profile. This will happen regardless of the dimensions of the rod or the magnitude of the electric field applied, and a complete analytic expression for this behavior is attainable using Laplace transforms. In the void, a similar situation applies and Ampere's law says that B_θ should behave approximately like $\frac{\mu_0 I(t)}{2\pi r}$ for all time, where $I(t)$ is the current in the rod and r is the distance from the z axis. However, this is merely the leading order solution for zero conductivity in the void. We also want to demonstrate a robust solution methodology when the conductivity in the void is non-zero. The B_θ formulation is unable

to handle zero-valued conductivity, so we set the void conductivity to be very small relative to the conductivity of the rod (e.g. $\frac{\sigma_v}{\sigma_r} \approx 10^{-6}$). The ramification is that now the solution in the void region is perturbed, making the analytic solution more difficult to derive. We could still, in principle, solve the inner-outer region exact solution via transform techniques for a constant electric field boundary condition at $r = b$ but this is unnecessary, and would not provide much additional value; so instead, we choose the electric field we desire at the interface $r = a$, for which we have a simple exact solution, and then compute the electric field boundary condition for the interface at $r = b$ that will impose it. This will provide an excellent verification of ALEGRA's ability to perform properly on a time dependent problem with a conductivity jump in an axisymmetric geometry. We focus first on the exact solution in the rod, which we can solve for using Laplace transforms and residue theory. Subsequently, we present first a perturbation solution in the void which matches boundary conditons at $r = a$ according to the perturbation approach. This will be followed by a derivation of an exact solution in the void extended directly term by term from the exact solution in the rod. These solutions are used to analyze the performance of the discrete numerical methods.

The Solution for B_θ in the Rod

Consider a thin rod of radius a as depicted in Figure 3.1. It is convenient to solve this problem using the vector potential form of the equations, so we begin with boundary value problem 3.1:

$$\begin{aligned} \nabla \times \nabla \times \mathbf{A} &= \mu_0 \sigma_r \left(-\frac{\partial \mathbf{A}}{\partial t} - \nabla \phi \right) \\ \phi(z=0) = 0; \quad \phi(z=h) = -V; \quad \nabla \phi \cdot \mathbf{n}(r=a) &= 0 \\ \mathbf{A} \times \mathbf{n} &= 0 \quad \text{on all surfaces} \end{aligned} \tag{3.1}$$

where $\mathbf{B} = \nabla \times \mathbf{A}$. Specializing to axial symmetry for A_z and imposing the Coulomb gauge $\nabla \cdot \mathbf{A} = 0$, we obtain

$$\frac{1}{\mu_0 \sigma_r} \frac{1}{r} \frac{\partial}{\partial r} \left(r \frac{\partial A_z}{\partial r} \right) = \frac{\partial A_z}{\partial t} - \frac{V}{h} \tag{3.2}$$

where $\frac{1}{\mu_0 \sigma_r}$ is the magnetic diffusivity. Applying a Laplace transform we get,

$$\frac{1}{\mu_0 \sigma_r} \frac{1}{r} \frac{\partial}{\partial r} \left(r \frac{\partial \hat{A}_z}{\partial r} \right) = u \hat{A}_z - \frac{V}{hu} \tag{3.3}$$

which, upon closer inspection, is recognized as a modified Bessel equation with u as the Laplace transform variable. A general solution for this partial differential equation (PDE) has the form:

$$\hat{A}_z = c_1 I_0(\sqrt{\mu_0 \sigma_r} u r) + c_2 K_0(\sqrt{\mu_0 \sigma_r} u r) + \hat{A}_{z,p} \tag{3.4}$$

where $\hat{A}_{z,p}$ is a particular solution of the PDE, I_0 and K_0 are the modified Bessel functions of the first and second kind, respectively, of order 0, and $c_1, c_2 \in \mathbf{R}$. Immediately we recognize that since K_0 has a logarithmic singularity at $r = 0$, we must have $c_2 = 0$. We also realize that the right-hand-side of 3.3 is independent of r, so a constant particular solution is a viable solution. The result is

$$\begin{aligned} 0 &= u\hat{A}_{z,p} - \frac{V}{hu} \\ \hat{A}_{z,p} &= \frac{V}{hu^2}. \end{aligned} \tag{3.5}$$

We are able to find c_1 by satisfying the boundary condition $\hat{A}_z(r = a) = 0$:

$$c_1 I_0(\sqrt{\mu_0 \sigma_r} u a) + \frac{V}{hu^2} = 0$$

$$c_1 = \frac{-V}{I_0(\sqrt{\mu_0 \sigma_r} u a) h u^2}. \tag{3.6}$$

This gives us

$$\hat{A}_z = \frac{-V}{hu^2} \left(\frac{I_0(\sqrt{\mu_0 \sigma_r} u r)}{I_0(\sqrt{\mu_0 \sigma_r} u a)} - 1 \right).$$

We get A_z by applying the inverse Laplace transform and integrating via residue theory [1].

$$A_z = \frac{-\mu_0 \sigma_r V}{h} \left(\frac{(r^2 - a^2)}{4} - 2a^2 \sum_{n=1}^{\infty} \frac{e^{\frac{-k_n^2 t}{\mu_0 \sigma_r a^2}} J_0\left(\frac{k_n r}{a}\right)}{k_n^3 J_0'(k_n)} \right) \tag{3.7}$$

where k_n is the n^{th} root of J_0. Finally, the axial magnetic flux, B_θ, is given by

[1] See appendix A for details

$$B_\theta = -\frac{\partial A_z}{\partial r} = \frac{\mu_0 \sigma_r V}{h}\left(\frac{r}{2} - 2a\sum_{n=1}^{\infty}\frac{e^{\frac{-k_n^2 t}{\mu_0\sigma_r a^2}} J_0'\left(\frac{k_n r}{a}\right)}{k_n^2 J_0'(k_n)}\right). \tag{3.8}$$

As a check, notice that as t approaches infinity, B_θ goes to a linear profile, which is what is expected.

A Perturbation Solution in the Void

We now need to obtain a solution in the void region that is consistent with the inner solution for non-zero σ_v. Since σ_v is very small, one would think that a perturbation analysis may be sufficient, as it also clearly provides insight into the physics of the problem. From a physical point of view, if the void conductivity is very small, it is clear that the outer region might be considered in quasi-steady state. We, thus, implicitly assume that we are only interested in time scales longer than the diffusion time across the void region and that these early transients may be ignored. Therefore, we can further assume that the solution may be given sequentially as

$$A_z^v = A_0 + \mu_0\sigma_v A_1 + \mu_0^2\sigma_v^2 A_2 + \cdots$$

$\mu_0\sigma_v$ is small.[2] Since σ_v very small relative to σ_r we expect that two terms will be sufficient for our perturbation solution.

Matching up terms of the same order we find that for the first equation

$$\frac{1}{r}\frac{\partial}{\partial r}\left(r\frac{\partial A_0}{\partial r}\right) = 0$$

which is easily solved, resulting in

$$A_0 = c\ln(r) + d \tag{3.9}$$

where c and d are constant with respect to r but may depend on time. In order to satisfy continuity of magnetic field with the inner solution we must have

$$c = \frac{\mu_0 I(t)}{2\pi}$$

since we have

$$B_0 = -\frac{\partial A_0}{\partial r} = \frac{\mu_0 I(t)}{2\pi r}$$

[2]Note that we could give a formal analysis in terms of a non-dimensional small parameter σ_v/σ_r but this informal approach is sufficient and clear enough for our purposes.

at $r = a$. The constant electric field at $r = a$, provides for a zero boundary condition on A_0 that we can use to solve for d. For this condition to hold,

$$d = \frac{\mu_0 I(t)}{2\pi} \ln(a).$$

and

$$A_0 = -\frac{\mu_0 I(t)}{2\pi} \ln(r) + \frac{\mu_0 I(t)}{2\pi} \ln(a) = -\frac{\mu_0 I(t)}{2\pi} \ln\left(\frac{r}{a}\right). \tag{3.10}$$

The next order equation in the pertubation expansion is

$$\frac{1}{r}\frac{\partial}{\partial r}\left(r\frac{\partial A_1}{\partial r}\right) = \left(\frac{\partial A_0}{\partial t} - \frac{V}{h}\right) \tag{3.11}$$

Substituting in A_0, Equation 3.11 becomes

$$\frac{1}{r}\frac{\partial}{\partial r}\left(r\frac{\partial A_1}{\partial r}\right) = -\frac{\mu_0 \dot{I(t)}}{2\pi} \ln\left(\frac{r}{a}\right) - \frac{V}{h}. \tag{3.12}$$

We solve this the same way as we did for A_0, and, applying the perturbation boundary conditions $\frac{\partial A_1}{\partial r}(r = a) = 0$ and $A_1(r = a) = 0$, we get

$$A_1 = -\frac{\mu_0 \dot{I}(t)}{2\pi}\left(\frac{r^2}{4}\ln\left(\frac{r}{a}\right) - \frac{r^2}{4} + \frac{a^2}{4}\ln\left(\frac{r}{a}\right) + \frac{a^2}{4}\right) - \frac{V}{2h}\left(\frac{r^2}{2} - \frac{a^2}{2} - a^2\ln\left(\frac{r}{a}\right)\right). \tag{3.13}$$

Therefore,

$$B_1 = \frac{\mu_0 \dot{I}(t)}{2\pi}\left(\frac{r}{2}\ln\left(\frac{r}{a}\right) - \frac{r}{4} + \frac{a^2}{4r}\right) + \frac{V}{2h}\left(r - \frac{a^2}{r}\right), \tag{3.14}$$

and

$$\begin{aligned} B_\theta = -\frac{\partial A_z}{\partial r} &= -\frac{\partial}{\partial r}\left(A_0 + \mu_0\sigma_r A_1\right) \\ &= B_1 + \mu_0\sigma_v B_1 \\ &= \frac{\mu_0 I(t)}{2\pi r} + \mu_0\sigma_v\left[\frac{\mu_0 \dot{I}(t)}{2\pi}\left(\frac{r}{2}\ln\left(\frac{r}{a}\right) - \frac{r}{4} + \frac{a^2}{4r}\right) + \frac{V}{2h}\left(r - \frac{a^2}{r}\right)\right] \end{aligned} \tag{3.15}$$

is our final result. This, with our previously derived solution for B_θ in the rod, makes a complete, analytic solution suitable for verification analysis.

All that remains is the derivation of the boundary condition at $r = b$ that produces the desired electric field at $r = a$. The electric field in the void is

$$\begin{aligned} E &= \frac{V}{h} - \frac{\partial A_z}{\partial t} \\ &= \frac{V}{h} + \frac{\mu_0 \dot{I}(t)}{2\pi} \ln\left(\frac{r}{a}\right) + \mu_0 \sigma_v \left[\frac{\mu_0 \ddot{I}(t)}{2\pi} \left(\frac{r^2 + a^2}{4} \ln\left(\frac{r}{a}\right) - \frac{r^2}{4} + \frac{a^2}{4} \right) \right]. \end{aligned} \tag{3.16}$$

When evaluated at $r = b$, this equation gives us our desired boundary condition.

Note that the solution in the void has terms which are proportional to the time derivatives of the total current in the rod, $I(t)$, which has the relationship $I(t) = \frac{2\pi a}{\mu_0} B_\theta(a,t)$. Expressions for these values are given in Equations 3.17, 3.18 and 3.19.

$$I(t) = \frac{\pi a^2 \sigma_r V}{h} \left(1 - 4 \sum_{n=1}^{\infty} \frac{e^{-\frac{k_n^2}{\mu_0 \sigma_r a^2} t}}{k_n^2} \right) \tag{3.17}$$

$$\dot{I}(t) = \frac{4\pi V}{\mu_0 h} \left(\sum_{n=1}^{\infty} e^{-\frac{k_n^2}{\mu_0 \sigma_r a^2} t} \right) \tag{3.18}$$

$$\ddot{I}(t) = \frac{4\pi V}{\mu_0^2 h \sigma_r a^2} \left(\sum_{n=1}^{\infty} k_n^2 e^{-\frac{k_n^2}{\mu_0 \sigma_r a^2} t} \right). \tag{3.19}$$

We would expect an initial condition $B_\theta(r,0) = 0$ which holds for the first term in the expansion Equation 3.15, but the next term depends on $\dot{I}(t)$, which is singular at $t = 0$ so that clearly the expansion has non-uniform validity in time. This is a clue that the perturbation theory approach for generating a comparison solution for this specific problem may not provide all that is desired.

Verification Study Details

We set up our model as a 1 mm long cylindrical rod with a 2 mm radius, a 3 mm deep void (see Figure 3.2), and a 1000 V/m electric field maintained on the surface of the rod. We use Equation 3.16 to produce a boundary condition at $r = b$ (see Figure 3.3) that should produce the same effect in ALEGRA as if we applied the electric field directly to the surface of the rod. For the electrical conductivity of the rod we choose $\sigma_r = 1$ MΩ·m, and for the electrical conductivity of the void we chose $\sigma_r = 1.0$ Ω·m.

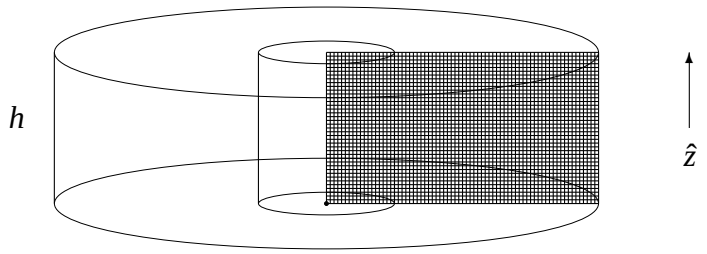

Figure 3.2: ALEGRA 2D (r,z) Cross Section

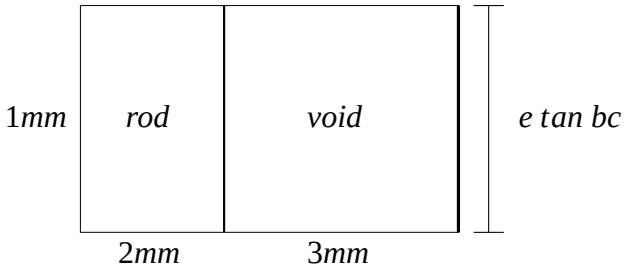

Figure 3.3: 2D (r,z) mesh with boundary condition on right side

For our mesh, we create two blocks, one representing the rod and another representing the void. This allows us to ensure that the conductivity jump is on the boundaries of elements regardless of how many elements we want to use. We set each block to have only one element in the z direction, and allow the number of elements in the r or s direction to vary. Because we anticipate the PSI-S formulation to converge very quickly, we set the first mesh in our study to have one element per block in the r or s direction. Thus, our very first mesh has exactly two elements. The strategy we employ for increasing the mesh size is to double the number of elements per block, per test.

In order to get ALEGRA to produce easily interpreted results, we impose a condition on the time steps ALEGRA uses to perform its calculations. The theoretical leading order error in ALEGRA's discrete solution is $O(\Delta t) + O((\Delta r)^2)$, where Δt is the time step used in the calculation, and Δr (or Δs) is the length of a mesh element in the r (or s) direction. So by forcing $\Delta t \propto (\Delta r)^2$, we make our error $O((\Delta r)^2) + O((\Delta r)^2) = O((\Delta r)^2)$, which allows us to confidently expect an order 2 rate of convergence for these tests. We do this by making some careful observations and choices when setting up our tests in ALEGRA.

Let N_s denote the smallest number of elements we use in our convergence analysis, if we double the number of elements for each subsequent test, then we may say that the i^{th} test in our convergence analysis will have $N_s \cdot 2^i$ elements per block. It follows that the lengths of the elements

decrease by half every subsequent test, so we may write: $\Delta r = \frac{1}{2^i}, i \in \mathbf{N}$. Now let N_i denote the number of elements in the i^{th} test, so $\Delta r = \frac{N_s}{N_i} = \frac{1}{2^i}$, we now desire $\Delta t = c(\Delta r)^2$ for some constant c. Theoretically, our choice of c is arbitrary, but working with a numerical method constrains our choice. The time step needs to always be small enough to allow ALEGRA to accurately capture interesting phenomena, but it also needs to be large enough to assure that our numerical method finishes its calculation in a reasonable amount of time. We see that when $i = 1$, then $\Delta t = c$ seconds, which helps us figure an upper bound on c. The diffusion time for the magnetic flux is roughly $\mu_0 \sigma_r a^2 = (4\pi \times 10^{-7})(1 \times 10^6)(0.002)^2 = 5.03 \times 10^{-6}$, so a safe choice seems to be $c = 0.5 \times 10^{-6}$. This ensures that Δt is small enough for ALEGRA to produce good results, but is still large enough that we can increment i several times before Δt becomes too small for ALEGRA to run efficiently. In addition, we can use this time step as the smallest comparison time because it is early in the transient phase of our test problem, but far enough along for us to observe interesting results.

Finally, we must carefully choose ALEGRA's method of output. We choose to use ALEGRA's capability to output data by cycle to ensure that we obtain the data we desire. Notice that

$$(\Delta r)^{-2}\Delta t = (\Delta r)^{-2}(0.5 \times 10^{-6})(\Delta r)^2 = 0.5 \times 10^{-6}$$

so, every $(\Delta r)^{-2} = 2^{2i}$ cycles, ALEGRA computes 0.5×10^{-6} seconds worth of data. Therefore, we have ALEGRA emit an output every $(\Delta r)^{-2}\Delta t$ cycles per test until the final time is reached, resulting in comparable data every 0.5 μs. Around 30 μs, the simulation begins approaching steady state, so we set the termination cycle to be $6 \times (\Delta r)^{-2}\Delta t$ cycles, which ends the simulation at that time.

Larger data sets can obtained with this method by dividing the time step above by factors of 10 and multiplying the number of cycles to termination by the same factor of 10. *We use a single factor of 10 when we perform these calculations.*

Convergence Results Using the Perturbation Solution

Figures 3.4, 3.5, and 3.6 show profile plots of B_θ for the different formulations as well as a tables showing the convergence rates measured for each mesh size using the L_2 norm. The black line represents the analytic solution we derived previously. Each result is given at time $t = 1.5$ μs, which is fairly representative of our general results and is still in the transient phase of problem. Also, each plot represents nodal data from nodes located at the bottom of the mesh ($z = 0.0$). We could also look at the nodal data at the top of the mesh or the elemental data at the center of the mesh, but nodal values are more accurate, and, since we have essentially made this problem one dimensional by having only one element in the z direction, we are able to accurately represent the overall results by only examining this set of nodes.

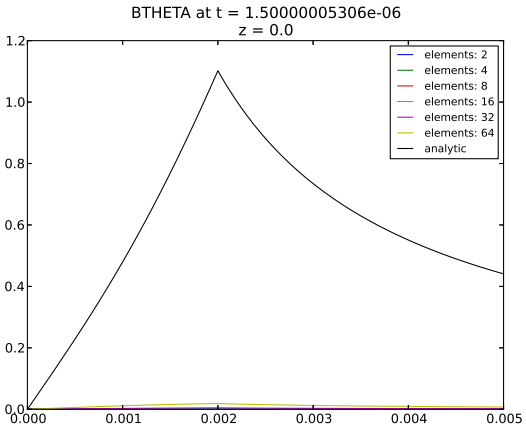

Number of elements per block	Order of convergence
1	2.09611e-01
2	2.09611e-01
4	7.31077e-02
8	2.16658e-02
16	1.01580e-02
32	2.09721e-02

Figure 3.4: B_θ profile for FIFE formulation at $t = 1.5$ μs

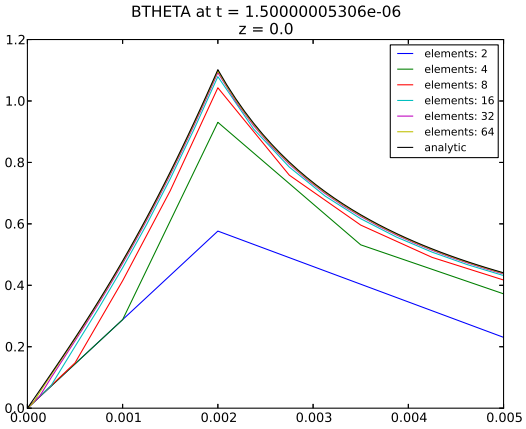

Number of elements per block	Order of convergence
1	1.52564e+00
2	1.52564e+00
4	1.43740e+00
8	1.35715e+00
16	1.29348e+00
32	1.22582e+00

Figure 3.5: B_θ profile for R-Scaled formulation at $t = 1.5$ μs

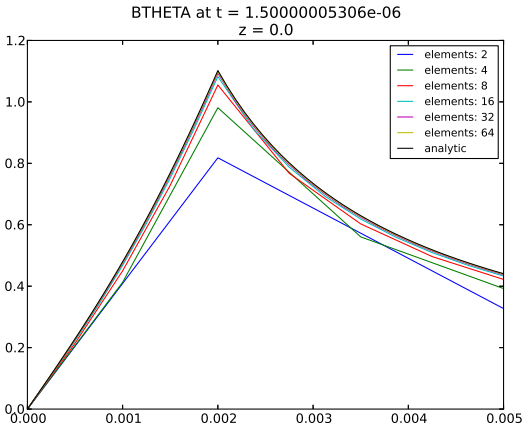

Number of elements per block	Order of convergence
1	1.40072e+00
2	1.40072e+00
4	1.38177e+00
8	1.27804e+00
16	1.16535e+00
32	1.07729e+00

Figure 3.6: B_θ profile for PSI-S formulation at $t = 1.5$ μs

We can see that FIFE formulation does not converge at all for these mesh resolutions (the largest

two mesh resolutions are barely distinguishable at the bottom of the plot). As a matter of fact, we do not see convergence for this formulation at all until we have mesh resolutions of thousands of elements[3]. This slow overall convergence is what makes the FIFE formulation impractical for this type of problem.

The R-Scaled formulation does better, but seems to be converging at an order one rate of convergence instead of order two. We see the same with the PSI-S formulation. This is not what we expected. To check our work, we construct two variations of our test. For the first variation, we perform the same test but with the void block removed. For the second, instead of driving the problem with an electric field boundary condition, we use a magnetic field boundary condition proportional to total current.

Convergence Results Without the Void

In this variation we completely omit the void block from the problem and see if we can see second order convergence. Our boundary condition now is simply a constant axial electric field set to 1000 V/m applied to the surface of the rod. The result appears to be second order convergence for the FIFE formulation as well as for the PSI-S formulation. The R-Scaled formulation appears to converge at a less than second order rate. We attribute this slower convergence rate to the inaccuracies near $r = 0$ rather than a problem with the code or the test, and note that the R-Scaled formulation could be converging even slower than what is seen here. These results are shown in Figures 3.7, 3.8, and 3.9. They suggests that ALEGRA handles this problem easily without the jump in conductivity and that the PSI-S code is behaving as it should.

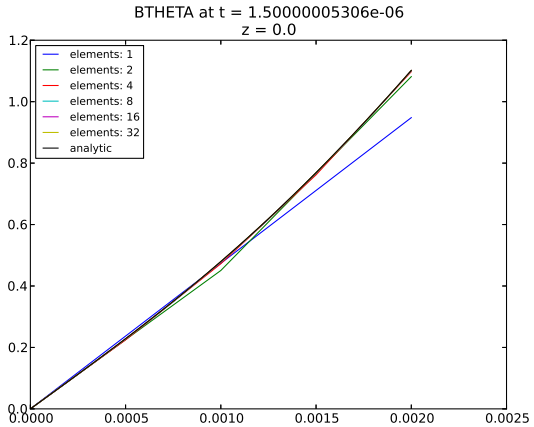

Number of elements per block	Order of convergence
1	2.24155e+00
2	2.24155e+00
4	2.01587e+00
8	2.02937e+00
16	2.00407e+00
32	2.00087e+00

Figure 3.7: B_θ profile for FIFE formulation without void at $t = 1.5$ μs

[3]See Appendix B

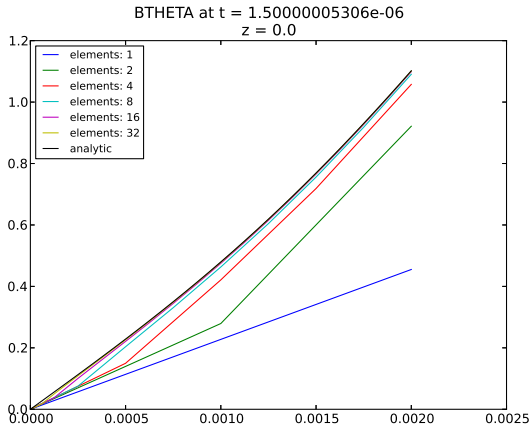

Number of elements per block	Order of convergence
1	1.44446e+00
2	1.44446e+00
4	1.55053e+00
8	1.50431e+00
16	1.46877e+00
32	1.45922e+00

Figure 3.8: B_θ profile for R-Scaled formulation without void at $t = 1.5$ μs

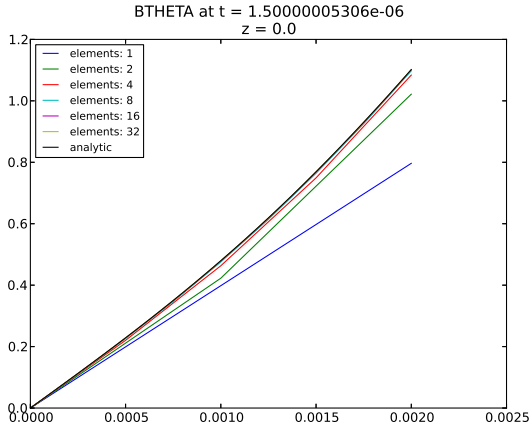

Number of elements per block	Order of convergence
1	1.92517e+00
2	1.92517e+00
4	1.92309e+00
8	1.97966e+00
16	1.99742e+00
32	2.00047e+00

Figure 3.9: B_θ profile for PSI-S formulation without void at $t = 1.5$ μs

Convergence Results with a Magnetic Field Boundary Condition

In the second variation, we use a magnetic field boundary condition proportional to the total current, $I(t)$, instead of Equation 3.16. The result is the use of a Dirichlet boundary condition to solve the magnetic diffusion equations instead of a Neumann boundary condition. This boundary condition is computed using Equation 3.20, and is entered into ALEGRA via a radial slot boundary condition. This method appears to provide much better control over the solution as seen in Figures 3.10, 3.11, and 3.12 and second order convergence rates are observed. We may thus conclude that the ALEGRA coding is correct, and that there must be another reason that we are not seeing second order convergence in the electric field drive case.

$$I(b,t) = \frac{2\pi r B_\theta(b,t)}{\mu_0} \tag{3.20}$$

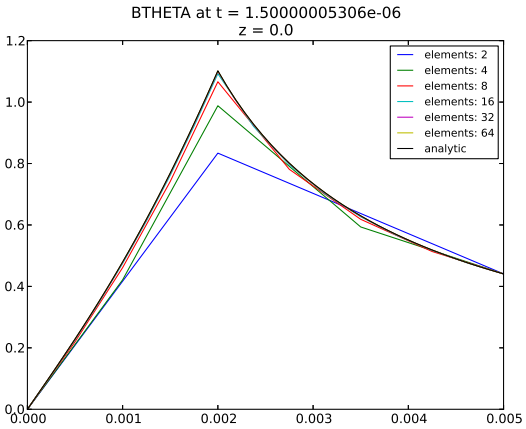

Number of elements per block	Order of convergence
1	1.52985e+00
2	1.52985e+00
4	1.78810e+00
8	1.93420e+00
16	1.98230e+00
32	1.99549e+00

Figure 3.10: B_θ profile for current driven FIFE formulation at $t = 1.5$ μs

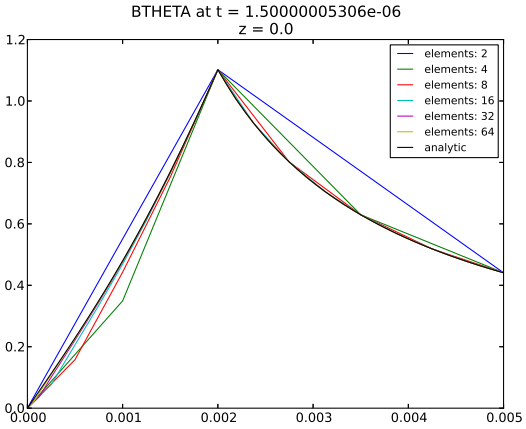

Number of elements per block	Order of convergence
1	-1.40915e+00
2	-1.40915e+00
4	1.17852e+00
8	1.27983e+00
16	1.34244e+00
32	1.39164e+00

Figure 3.11: B_θ profile for current driven R-Scaled formulation at $t = 1.5$ μs

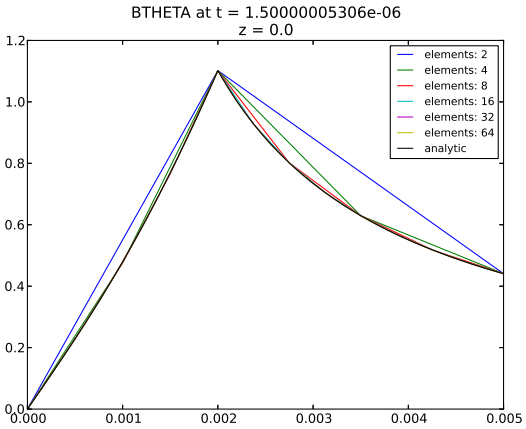

Number of elements per block	Order of convergence
1	-1.11351e+01
2	-1.11351e+01
4	6.21110e-02
8	1.73137e+00
16	1.94386e+00
32	1.99100e+00

Figure 3.12: B_θ profile for current driven PSI-S formulation at $t = 1.5$ μs

We conclude that the problem is the approximate analytic solution. We can see that Equations

3.15 and 3.16 both depend on derivatives of $I(t)$, which are singular at $t = 0$, so some inaccuracies can be expected from these equations. In this case, it seems that these inaccuracies are significant enough to disrupt our verification analysis. The remedy, then, is a new analytic solution without these issues.

An exact solution in the void

We now realize that we need a more precise solution which matches the solution in the rod very carefully at $r = a$. In a certain sense, we need to manufacture an exact solution which has the same character, but precisely matches the required boundary conditions for all time. We assume that our analytical solution for B_θ in the rod holds, and use it to manufacture a solution for B_θ in the void by again matching continuous magnetic and electric fields to our interior solution at the interface $r = a$. The solution for B_θ in the rod is exactly the same and we go directly to solving an expression for B_θ in the void region. Thereafter, we will derive the corresponding initial and boundary conditions.

The general method of manufactured solutions [9] typically solves $g = Du$ for g, where D is a differential operator, u is some exact solution, and g is a source term stemming from the exact solution. In the approach described below, we use a special form of this method, which allows us to carefully choose the solution u so that we have no source term to solve for (i.e. $g = 0$). We suggest that this general approach of extending solutions using fundamental solutions from a separation of variables approach might be useful in other verification contexts.

Consider again Figure 3.1. We desire to manufacture a complete solution for the void region which is consistent with the inner solution and free of singularities. We recognize the following PDE

$$\frac{1}{r}\frac{\partial}{\partial r}\left(r\left(-\frac{1}{\mu}\frac{\partial A_z}{\partial r}\right)\right) = \sigma\left(-\frac{\partial A_z}{\partial t} + \frac{V}{h}\right) \tag{3.21}$$

as a form of Bessel's equation, and note that a general solution is:

$$\begin{aligned} A_z = &-\frac{\mu\sigma V}{4h}r^2 + c_1\mu log(r) + c_2 \\ &+ \sum_{n=1}^{\infty} e^{-\frac{\lambda_n^2}{\mu\sigma}t}\left[a_n J_0(\lambda_n^2 r) + b_n Y_0(\lambda_n^2 r)\right] \end{aligned} \tag{3.22}$$

where c_1, c_2, a_n, b_n, $\lambda_n \in \mathbf{R}$ are constants determined by boundary and initial conditions, and J_0 and Y_0 are Bessel functions of the first and second kind, respectively of order zero. Consider the cross section shown in Figure 3.13.

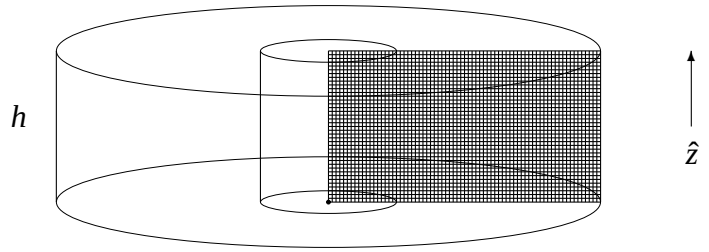

Figure 3.13: 3D View of Test Problem in (r,z) with Outlined Cross Section

As shown in Figure 3.14, this depicts a two dimensional cross-section of a rod of radius a and height h, in a void of thickness $b-a$.

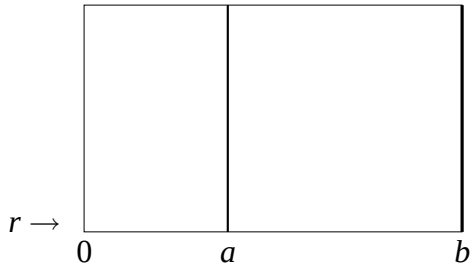

Figure 3.14: 2D (r,z) Cross Section

On the interval $0 \leq r \leq a$, we already have a solution via Laplace transform:

$$A_z = -\frac{\mu\sigma V}{h}\left[\frac{(r^2-a^2)}{4} - 2a^2\sum_{n=1}^{\infty}\frac{e^{-\frac{k_n^2 t}{\mu\sigma a^2}}J_0\left(\frac{k_n r}{a}\right)}{k_n^3 J_0'(k_n)}\right] \tag{3.23}$$

We desire to extend this solution into $a \leq r \leq b$. Because we are manufacturing an analytic solution, we can choose all the constants in the general solution in the void as we please, but because we also want our solution to be an extension of Equation 3.23, the two solutions must satisfy the physical jump conditions, i.e. continuity of tangential electric and magnetic fields. These two sets of conditions allow us to find a complete solution to B_θ in the void consistent with the solution in the rod. From here forward, we move away from the designation of the rod and void, and instead derive the following equation with arbitrary material parameters. A superscript L will denote a

reference to variables and equations on the left side of $r = a$, and a superscript R will denote a reference to variables and equations on the right side, as shown in Equations 3.24 and 3.25.

$$A_z^L(r=a,t) = A_z^R(r=a,t) \tag{3.24}$$

$$-\frac{1}{\mu_L}\frac{\partial A_z^L}{\partial r}(r=a,t) = -\frac{1}{\mu_R}\frac{\partial A_z^R}{\partial r}(r=a,t) \tag{3.25}$$

We first consider how to achieve consistent matching time scales variation and then complete the derivation by matching the jump conditions term by term in Equation 3.23.

Consistency of Time Dependence

The time dependent part of both solutions is located within the exponentials, forcing the condition

$$e^{-\frac{(\lambda_n^L)^2 t}{\mu^L \sigma^L}} = e^{-\frac{(\lambda_n^R)^2 t}{\mu^R \sigma^R}} \tag{3.26}$$

where $\lambda_n^L = \frac{k_n}{a}$. This leads to the requirement:

$$\lambda_n^R = \sqrt{\frac{\mu^R \sigma^R k_n^2}{\mu^L \sigma^L a^2}}. \tag{3.27}$$

This is the only condition imposed by consistency of time dependence.

Jump Conditions

The rest of the constants, c_1, c_2, a_n, and b_n, are chosen to satisfy the jump conditions Equations 3.24 and 3.25. These conditions fully expanded are given below.

$$\frac{\mu^L\sigma^L V}{h}\left[2a^2\sum_{n=1}^{\infty}\frac{e^{-\frac{k_n^2 t}{\mu^L\sigma^L a^2}}J_0(k_n)}{k_n^3 J_0'(k_n)}\right]$$
$$=\left(-\frac{\mu^R\sigma^R V}{4h}a^2+c_1\mu^R log(a)+c_2\right)$$
$$+\sum_{n=1}^{\infty}e^{-\frac{(\lambda_n^R)^2 t}{\mu_R\sigma^R}}\left[a_n J_0((\lambda_n^R)^2 a)+b_n Y_0((\lambda_n^R)^2 a)\right] \tag{3.28}$$

$$-\frac{1}{\mu^L}\left[-\frac{\mu^L\sigma^L V}{h}\left(\frac{a}{2}-2a\sum_{n=1}^{\infty}\frac{e^{-\frac{k_n^2 t}{\mu^L\sigma^L a^2}}J_0'(k_n)}{k_n^2 J_0'(k_n)}\right)\right]$$
$$=-\frac{1}{\mu^R}\left[-\frac{\mu^R\sigma^R V}{2h}a+\frac{c_1\mu^R}{a}\right.$$
$$\left.+\sum_{n=1}^{\infty}e^{-\frac{(\lambda_n^R)^2 t}{\mu_R\sigma^R}}\lambda_n^2\left[a_n J_0'((\lambda_n^R)^2 a)+b_n Y_0'((\lambda_n^R)^2 a)\right]\right] \tag{3.29}$$

The steady state parts of these equations provide enough information to derive c_1 and c_2. c_1 is obtained first through Equation 3.29, resulting in Equation 3.30. Substituting Equation 3.30 into Equation 3.28 results in Equation 3.31.

$$c_1=\frac{(\sigma^R-\sigma^L)V}{2h}a^2 \tag{3.30}$$

$$c_2=\frac{\mu^R log(a)(\sigma^R-\sigma^L)V}{2h}-\frac{\mu^R\sigma^R V}{4h}a^2 \tag{3.31}$$

What remains are the values of a_n and b_n. Substituting Equations 3.27, 3.30, and 3.31 into Equations 3.28 and 3.29 and simplifying, we get the following two conditions on a_n and b_n:

$$\sum_{n=1}^{\infty}\left[a_n J_0\left(\frac{\mu_R\sigma^R k_n^2}{\mu^L\sigma^L a}\right)+b_n Y_0\left(\frac{\mu_R\sigma^R k_n^2}{\mu^L\sigma^L a}\right)\right]=0 \tag{3.32}$$

$$\sum_{n=1}^{\infty}\frac{\sigma^R k_n^2}{\mu^L\sigma^L a}\left[a_n J_0'\left(\frac{\mu_R\sigma^R k_n^2}{\mu^L\sigma^L a}\right)+b_n Y_0'\left(\frac{\mu_R\sigma^R k_n^2}{\mu^L\sigma^L a}\right)\right]=\frac{2\sigma^L V a}{h}\sum_{n=1}^{\infty}\frac{1}{k_n^2}. \tag{3.33}$$

Letting $\xi_n=\frac{\mu^R\sigma^R k_n^2}{\mu^L\sigma^L a}$, Equations 3.32 and 3.33 further simplify to Equations 3.34 and 3.35.

$$a_n J_0(\xi_n) + b_n Y_0(\xi_n) = 0 \qquad \forall n \tag{3.34}$$

$$a_n J_0'(\xi_n) + b_n Y_0'(\xi_n) = \frac{2\mu^L(\sigma^L)^2 V a^3}{\sigma^R k_n^4 h} \qquad \forall n \tag{3.35}$$

We now have a countably infinite set of two equations and two unknowns, each of which can be solved to find the corresponding a_n and b_n.

Let $\Phi_n = \begin{pmatrix} J_0(\xi_n) & Y_0(\xi_n) \\ J_0'(\xi_n) & Y_0'(\xi_n) \end{pmatrix}$, with $\underline{x}_n = \begin{pmatrix} a_n \\ b_n \end{pmatrix}$ and $\underline{b}_n = \begin{pmatrix} 0 \\ \frac{2\mu^L(\sigma^L)^2 V a^3}{\sigma^R k_n^4 h} \end{pmatrix}$.

Then our system can be described by $\Phi_n \underline{x}_n = \underline{b}_n$. Since this system is 2x2, as long as $det(\Phi_n) \neq 0$, Φ_n has an easily solvable inverse which can be used to find $\underline{x}_n$. In our case, we can show $det(\Phi_n) \neq 0$.

$\underline{det(\Phi_n) \neq 0}$

First we note that $J_0(x)$ and $Y_0(x)$ are the fundamental solutions to the Bessel equation

$$y'' + \frac{1}{x} y' + y = 0. \tag{3.36}$$

to which we can apply Abel's Theorem. This gives an expression for the Wronskian of 3.36, which is actually equal to $det(\Psi)(\xi_n)$. Abel's Theorem gives us

$$\begin{aligned} &W(J_0(x), Y_0(x)) \\ &\qquad = \left[J_0(a)Y_0'(a) - J_0'(a)Y_0(a)\right] exp\left(-\int \tfrac{1}{x} dx\right) \\ &\qquad = \left[J_0(a)Y_0'(a) - J_0'(a)Y_0(a)\right] \tfrac{1}{x} \end{aligned}$$

Since a is not a root of J_0, J_0', Y_0, or Y_0', $\left[J_0(a)Y_0'(a) - J_0'(a)Y_0(a)\right]$ is a constant, and since $\frac{1}{x}$ is never zero, $det(\Phi_n) = W(J_0(\xi_n), Y_0(\xi_n))$ is never zero.

Therefore, Φ_n^{-1} is given by $\frac{1}{J_0(\xi_n)Y_0'(\xi_n) - Y_0(\xi_n)J_0'(\xi_n)} \begin{pmatrix} Y_0'(\xi_n) & -Y_0(\xi_n) \\ -J_0'(\xi_n) & J_0(\xi_n) \end{pmatrix}$ and

$$\underline{x}_n = \Phi_n^{-1} \underline{b}_n = \frac{1}{J_0(\xi_n)Y_0'(\xi_n) - Y_0(\xi_n)J_0'(\xi_n)} \begin{pmatrix} -Y_0(\xi_n)\left(\frac{2\mu^L(\sigma^L)^2 a^3 V}{\sigma^R k_n^4 h}\right) \\ J_0(\xi_n)\left(\frac{2\mu^L(\sigma^L)^2 a^3 V}{\sigma^R k_n^4 h}\right) \end{pmatrix}.$$

Thus, a_n and b_n are given by:

$$a_n = -\left(\frac{2\mu^L(\sigma^L)^2a^3V}{\sigma^R k_n^4 h}\right)\frac{Y_0(\xi_n)}{J_0(\xi_n)Y_0'(\xi_n) - Y_0(\xi_n)J_0'(\xi_n)} \tag{3.37}$$

$$b_n = \left(\frac{2\mu^L(\sigma^L)^2a^3V}{\sigma^R k_n^4 h}\right)\frac{J_0(\xi_n)}{J_0(\xi_n)Y_0'(\xi_n) - Y_0(\xi_n)J_0'(\xi_n)} \tag{3.38}$$

$$\xi_n = \frac{\mu^R\sigma^R k_n^2}{\mu^L\sigma^L a} \tag{3.39}$$

Final Solution

We now have all the information we need to write out an analytic solution for B_θ in the void.

$$\begin{aligned} B_\theta^R &= -\frac{\partial A_z^R}{\partial r} \\ &= \frac{\mu^R\sigma^R V}{2h}r - \frac{c_1\mu^R}{r} - \sum_{n=1}^{\infty}(\lambda_n^R)^2 e^{-\frac{(\lambda_n^R)^2 t}{\mu^R\sigma^R}}\left[a_n J_0'((\lambda_n^R)^2 r) + b_n Y_0'((\lambda_n^R)^2 r)\right] \end{aligned} \tag{3.40}$$

where c_1, c_2, λ_n^R, a_n, and b_n are all given above. For our manufactured solution to be useful, we need a method of driving the solution in ALEGRA. The method we use as a driving force is the application of an initial condition and a boundary condition. We impose a B_θ field initial condition to the bottom of the mesh, and an electric field boundary condition on outside of the void (right side of the mesh) as we did before. The boundary condition and initial condition are given by:

$$\begin{aligned} E(b,t) &= \frac{V}{h} - \frac{\partial A_z}{\partial t}(b,t) \\ &= \frac{V}{h} + \frac{1}{\mu^R\sigma^R}\sum_{n=1}^{\infty}(\lambda_n^R)^2 e^{-\frac{(\lambda_n^R)^2 t}{\mu^R\sigma^R}}\left[a_n J_0((\lambda_n^R)^2 b) + b_n Y_0((\lambda_n^R)^2 b)\right] \end{aligned} \tag{3.41}$$

$$\begin{aligned} B_\theta(r,0) &= -\frac{\partial A_z}{\partial r} \\ &= \begin{cases} \frac{\mu^L\sigma^L V}{h}\left[\frac{r}{2} - 2a\sum_{n=1}^{\infty}\frac{J_0'(\frac{k_n r}{a})}{k_n^2 J_0'(k_n)}\right], & \text{if } r \le a \\ \frac{\mu^R\sigma^R V}{2h}r - \frac{\mu^R c_1}{r} - \sum_{n=1}^{\infty}(\lambda_n^R)^2\left[a_n J_0'((\lambda_n^R)^2 r) + b_n Y_0'((\lambda_n^R)^2 r)\right], & \text{if } r > a \end{cases} \end{aligned} \tag{3.42}$$

with $a = .002$,$b = .005$, and $h = .001$ as chosen parameters.

Convergence Results Using the Exact Solution

The set up for the exact solution convergence study is exactly the same as the perturbation solution case except that a new formula for computing the electric field boundary is required as well as specification of an initial condition, $B_\theta(r,0)$. We analyze and plot the results of our test with the manufactured solution the same way we did previously, and this time they meet our expectations.

As with the perturbation solution, Figure 3.15 shows that the FIFE formulation is not converging at this mesh resolution; however, in Appendix B we see that, with mesh resolutions of 100 to 3200, not only does the FIFE formulation converge, but it converges at a second order rate. We feel it is important to note that testing done previous to this study on this type of problem suggested that the FIFE formulation is second order convergent, but that very fine mesh resolutions was needed to see this behavior.

On the other hand, Figure 3.16 shows that the R-Scaled formulation appears to be approaching a convergence rate of about 1.4, which we learned from our simplified problems is expected. Finally, Figure 3.17 demonstrates the excellent convergence and accuracy of the PSI-S formulation, successfully concluding our verification analysis.

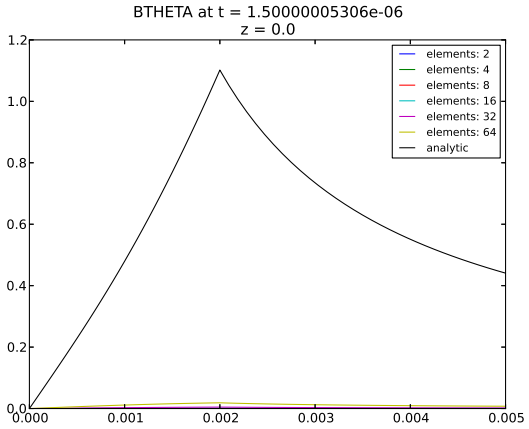

Number of elements per block	Order of convergence
1	2.09611e-01
2	2.09611e-01
4	7.31078e-02
8	2.16662e-02
16	1.01587e-02
32	2.09737e-02

Figure 3.15: FIFE formulation with manufactured solution at $t = 1.5$ μs

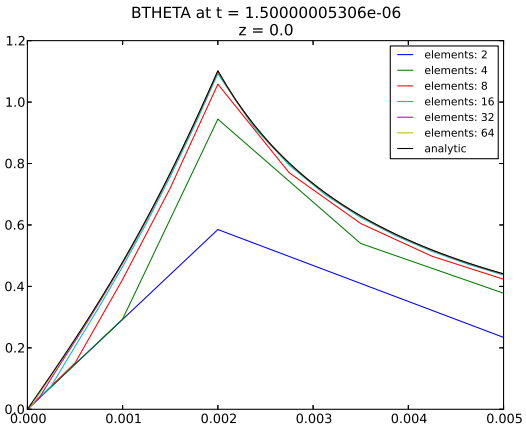

Number of elements per block	Order of convergence
1	1.59109e+00
2	1.59109e+00
4	1.60632e+00
8	1.66119e+00
16	1.53120e+00
32	1.45542e+00

Figure 3.16: R Scaled formulation with manufactured solution at $t = 1.5$ μs

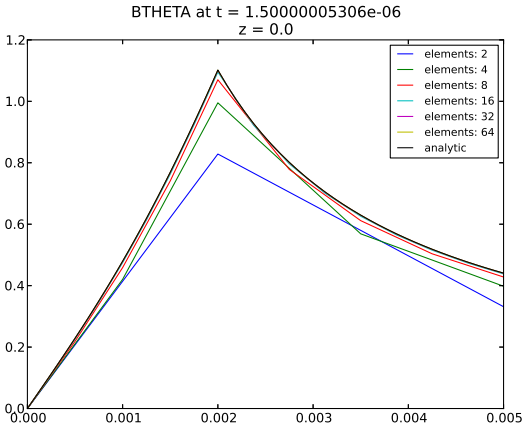

Number of elements per block	Order of convergence
1	1.52672e+00
2	1.52672e+00
4	1.75725e+00
8	2.24243e+00
16	2.33500e+00
32	2.03655e+00

Figure 3.17: PSI-S formulation with manufactured solution at $t = 1.5$ μs

Current Driven Test

We also include here the results of the magnetic field or current driven test. The only change required made for the manufactured solution version of this test are that the B_θ in Equation 3.20 is now the new manufactured solution, and we add the corresponding initial condition to the simulation setup. The results are not surprising. In Figures 3.19 and 3.20 we observe second order convergence for the FIFE and PSI-S formulations, and no better than order 1.4 convergence for the R-Scaled formulation.

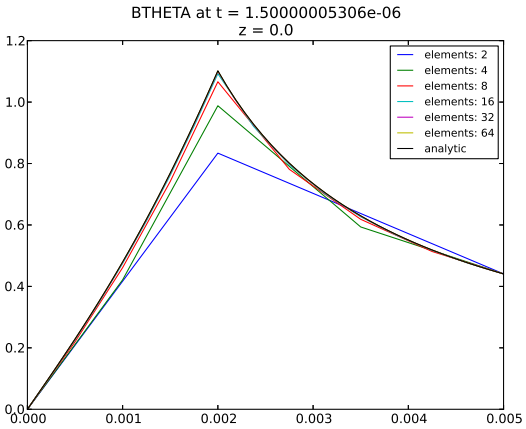

Number of elements per block	Order of convergence
1	1.52986e+00
2	1.52986e+00
4	1.78815e+00
8	1.93444e+00
16	1.98358e+00
32	2.00109e+00

Figure 3.18: Current driven FIFE formulation with manufactured solution at $t = 1.5$ μs

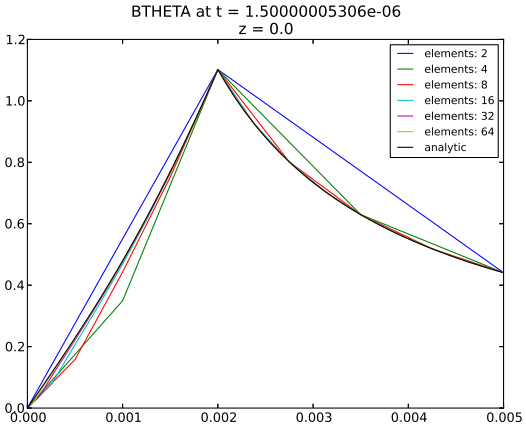

Number of elements per block	Order of convergence
1	-1.43285e+01
2	-1.43285e+01
4	1.17855e+00
8	1.27991e+00
16	1.34268e+00
32	1.39219e+00

Figure 3.19: Current driven R Scaled formulation with manufactured solution at $t = 1.5$ μs

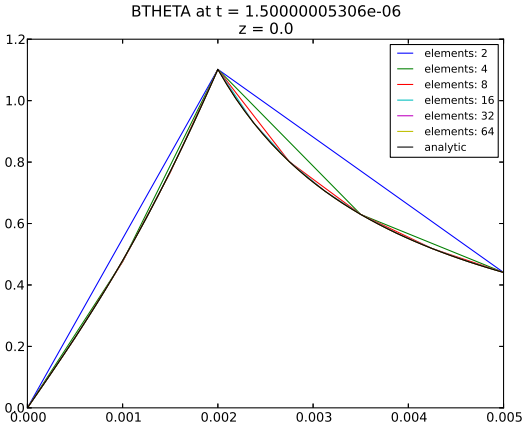

Number of elements per block	Order of convergence
1	-1.23872e+01
2	-1.23872e+01
4	6.24712e-02
8	1.73489e+00
16	1.96379e+00
32	2.08265e+00

Figure 3.20: Current driven PSI-S formulation with manufactured solution at $t = 1.5$ μs

Chapter 4

Examination of Additional Variables

We now discuss two significant improvements that have been observed with the PSI-S formulation. In particular we show benefits for computation of the current density and the Joule heating rate.

Current Density

The current density, $\mathbf{J}$, is given by the curl of the magnetic field and lies in the (r,z) plane. Thus

$$\mathbf{J} = \sigma\mathbf{E} = \nabla \times (\mathbf{B}/\mu_0) = J_r\hat{r} + J_z\hat{z} = -\frac{1}{\mu_0}\frac{\partial B_\theta}{\partial z}\hat{r} + \frac{1}{\mu_0}\frac{\partial (rB_\theta)}{r\partial r}\hat{z} \tag{4.1}$$

The ALEGRA 2D curl operator in axisymmetric coordinates is given by

$$\mathbf{J} = \sigma\mathbf{E} = \nabla \times (\mathbf{B}/\mu_0) = -\frac{1}{\mu_0}\frac{\partial B_\theta}{\partial z}\hat{r} + \frac{1}{\mu_0}\left(\frac{\partial B_\theta}{\partial r} + \frac{\bar{B_\theta}}{\bar{r}}\right)\hat{z} \tag{4.2}$$

where the bar notation $\bar{(\cdot)}$ indicates a nodal average and the partial derivatives are computed using the finite element gradient operator on nodal fields evaluated at the center of the reference coordinates linearly interpolating (r,z) coordinates.

Figure 4.1 shows a plot of J_z as a function of r at steady state. It is easily observed that there is a significant difference between the J_z values as computed by the R-Scaled formulation versus the J_z values as computed by Equation 4.4. We can verify that the PSI-S formulation is more accurate by the simple observation that, at steady state, the current density should be constant in the wire. The PSI-S formulation reflects this while the R-Scaled result does not.

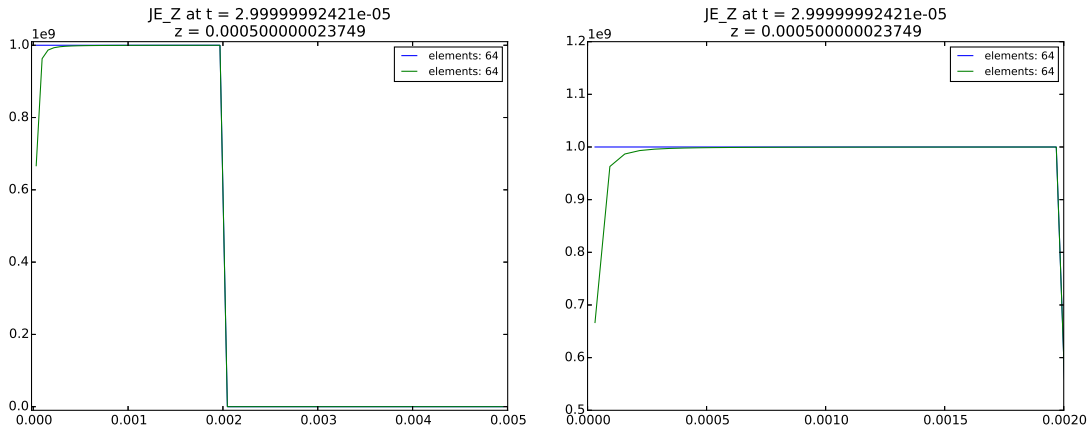

(a) Scale **(b)** Zoomed

Figure 4.1: R-Scaled (green) and PSI-S (blue) overlay of J_z

We also performed an initial scoping study of the quality of J_r. A useful test problem to this end is a wire in a void with a metal plate on the top and bottom of the mesh, and a constant H_θ boundary condition on the outside of the void between the two plates. The effect is an initial **J** field that diffuses into the wire and plates until eventually reaching steady state. We should be able to see that J_r becomes approximately, spatially and temporally constant in the metal plates away from the wire. Further, this constant value will be related to the boundary condition via the equation:

$$(2\pi r)h_p J_r = I_b \tag{4.3}$$

where h_p is the height (thickness) of the plate and I_b is the constant magnitude current associated with the boundary condition on the outside of the void at $r = b$. By running the problem long enough to be in steady state and measuring the magnitude of J_r at the center of the plate, we can verify that J_r is of the correct magnitude.

We choose a 4 mm long wire with a radius of 1 mm. We let the void be 4 mm deep, and we put 1 mm thick plates on the top on bottom of the mesh and utilize a spatial resolution of 6.25×10^{-5}m. We apply field corresponding to a constant current of $I_b = 1.0\ A$ on the outside of the void, zero tangential fields on the outer top and bottom z planes and default zero tangential electric field conditions on the radial surfaces of the plates. After running for 200 μs, we measure J_r to be 3.254×10^4 A/m^2 at $r = 4.9$ mm. Inserting these values into Equation 4.3, we get $J_r = 3.248 \times 10^4$ A/m^2 showing that the results are equivalent to better than 1 percent.

It is also possible to define an alternate formulation for the current density by considering (s,z) coordinates.

$$\mathbf{J} = -\frac{1}{\mu_0}\frac{\partial B_\theta}{\partial z}\hat{r} + \frac{2}{\mu_0}\frac{\partial \psi}{\partial s}\hat{z} \tag{4.4}$$

Again we can evaluate each of these terms using the standard finite element gradient operator transformed to (s,z) coordinates. Note that there are no terms proportional to $1/r$ or $1/s$ in this

formula so one might think that this formula would be preferable. We have not yet found any evidence for such a conclusion. Thus the difference shown above between the different formulation are result of differences in the flux density solution and not due to the curl operator implementation.

Joule heating

Using the weak form equations, ALEGRA computes a natural definition for the Joule heating. This results in a rise in temperature and thus also a rise in pressure through the equation of state. We can see in Figure 4.2 that the R-Scaled formulation has significantly different pressure values than the PSI-S formulation for the first 1-3 elements. The temperature variable is similar as can be seen in Figure 4.3. These visual results suggest that additional benefits in proper thermodynamic incremental behavior due to Joule heating are available with the PSI-S formulation.

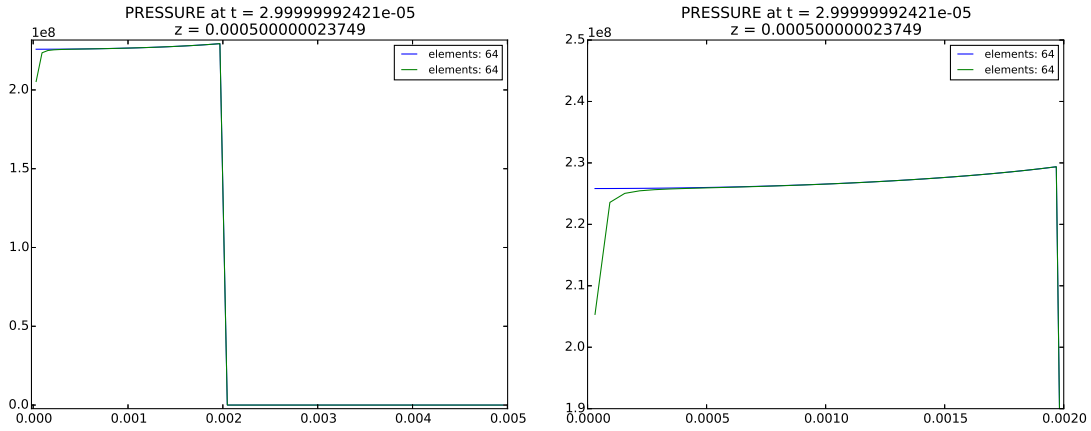

(a) Scale **(b)** Zoomed

Figure 4.2: R-Scaled (green) and PSI-S (blue) overlay of the PRESSURE variable

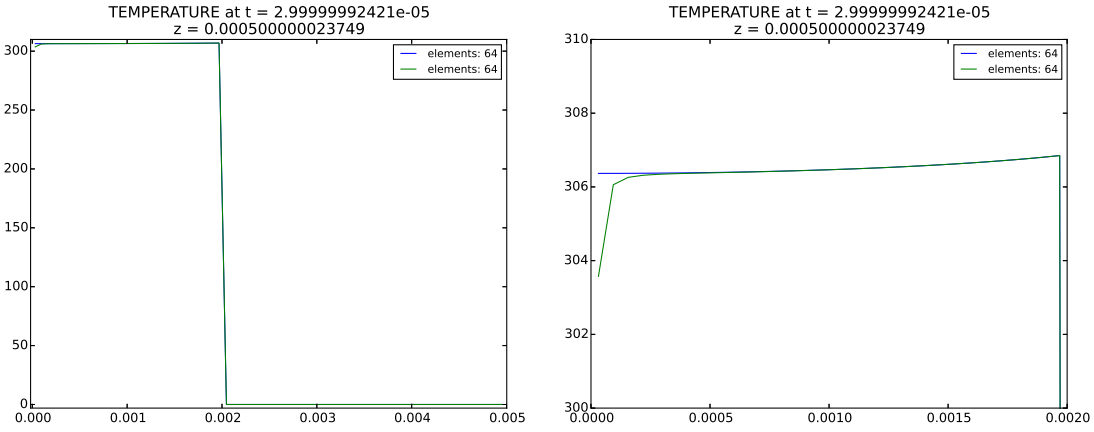

(a) Scale **(b)** Zoomed

Figure 4.3: R-Scaled (green) and PSI-S (blue) overlay of the TEMPERATURE variable

Chapter 5

A Relevant Validation Problem in Magnetohydrodynamics

While the verification study indicates that we have been successful in showing the advantages of the PSI-S formulation for verification problems, we are also interested in the performance of the method on larger, more complex problems. One such problem is an exploding wire. The exploding wire can be modeled as a 2D axisymmetric MHD problem with resulting dynamics that can become very complicated very quickly, making it an excellent test of performance for the PSI-S formulation.

In this chapter we will thoroughly describe our version of the exploding wire problem, run the simulation, and analyze the results with comparison to experimental data from exploding wire tests. We are particularly interested in discovering whether or not the validation study will show improvements suggested by the verification test problem, as well as any other differences between the results produced by the PSI-S formulation and those produced by the R-Scaled formulation.

Problem and Simulation Description

The exploding wire system considered here represents experiments described in References [2] and [4]. Previous modeling for these experiments using ALEGRA also appears in Reference [5]. The system is a capacitive discharge circuit which transfers stored electrical energy to thermal and kinetic energy, via extremely intense Ohmic heating of a metal filament. The filament is a narrow cylindrical wire, and broad steel electrode plates connect each end of the wire to the rest of the discharge circuit. The circuit is an RLC (resistor-inductor-capacitor) circuit, with resistance $R = 2\ \Omega$, inductance $L = 1.15\ \mu$H, capacitance $C = 1.88\ \mu$F, and initial capacitor charge voltage $V_0 = -19.98$ kV.

The ALEGRA simulations consist of a 2D axisymmetric computational domain, connected to a lumped-element circuit model, which is laid out as shown schematically in Figure 5.1(a). The ALEGRA mesh adds both resistance and inductance to the system, and the modeled circuit supplies electromagnetic energy to the simulation domain, which manifests itself as current appearing on the plates and in the wire. The circuit is coupled via time-dependent magnetic-field boundary conditions maintained at the outer radial boundary of the domain. This coupling is similar to the

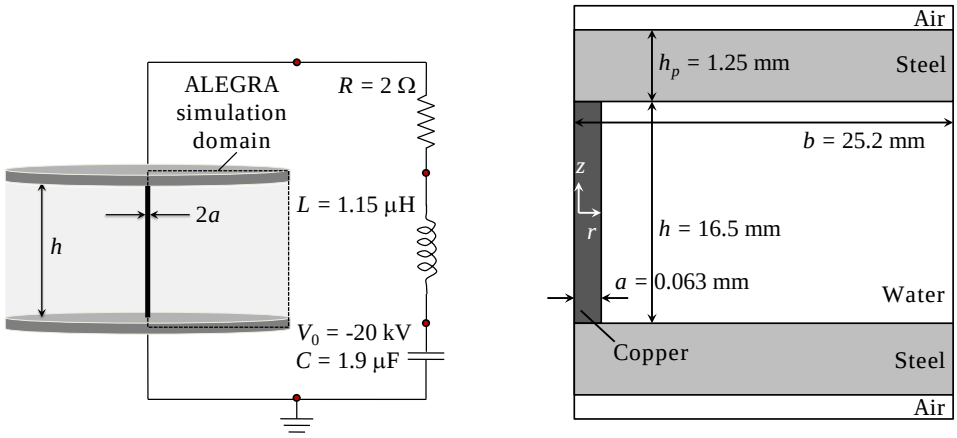

(*a*) (*b*)

Figure 5.1: Schematic diagrams (not to scale), showing (*a*) layout of circuit model driving the exploding wire simulations, and (*b*) details of the geometry used in the 2D ALEGRA simulation domain.

magnetic-field-driven verification problems of Chapter 3, in that the current density distribution develops naturally in time in response to imposed electromagnetic fields. However, here, resistive magnetohydrodynamics (MHD) is considered, rather than just transient magnetics. Further, the boundary conditions for the magnetic field are driven by the nonlinearly coupled circuit model, rather than a predefined current. In the simulation domain, the equations of resistive MHD are integrated forward in time, allowing the material and electromagnetic fields in the domain to evolve according to the energy supplied from the circuit. The material models for copper and steel both include Johnson-Cook strength models and Sesame equations of state 3320 and 4279 respectively, with temperatures limited to the range 50 K $\leq T \leq$ 50,000K. Lee-More-Desjarlais electrical conductivity models are also used, encoded in Sesame tables 29325 for copper and 29428 for steel [3].

A water-filled gap between the plates acts in similar fashion to the void used in the verification tests, forcing the current from the circuit to flow in highly concentrated fashion through the wire during the discharge event. This geometry, including the plates, wire, and air gap is shown schematically in Figure 5.1(*b*). Improvements to the underlying finite element formulation used in ALEGRA should affect solutions computed for this problem.

The concept of exploding wires has been studied extensively within a wide array of applications ranging from the generation of electromagnetic radiation to the collection of data for calibration of equation-of-state and conductivity models. [1, 13, 12, 7, 4, 2, 5, 11]. A significant body of experimental data exists for exploding wires of various materials in various environments. Data for this study were provided by George Vunni (US Army Research Laboratory), consisting of tabulated time-histories of the current and voltage drop across the load for three tests performed with copper wires as part of the study described in Reference [2].

The copper wires used in these experiments had a radius $a = 0.063$ mm and a length $h = 16.5$ mm. For this wire radius, assuming a nominal fixed copper resistivity of $\sigma = 50$ MΩ·m, the magnetic diffusion time would be approximately 0.25 μs, and the current density would therefore be relatively well-diffused by the time current has been flowing for 1 μs.

In the present study, the ALEGRA simulation is run on four computational meshes, at 15, 30, 60, and 120 elements per mm. This corresponds to 0.9, 1.9, 3.8, and 7.6 elements spanning the initial wire radius. We denote these cases here using N = 1, 2, 4, 8. The mesh is radially biased at large radii, but the mesh aspect ratio is restricted to aspect ratios of 4 or less. The resulting mesh sizes are 45,900, 184,200, 739,200, and 2,959,200 elements. The simulations are carried out using both the R-Scaled and PSI-S formulations and are run in parallel on Sandia's Skybridge cluster.

Behavior Near the Axis

To examine the effect of the axisymmetric formulation on the computed solution, we first examine the behavior of the B_θ field near $r = 0$. Figure 5.2 is a zoomed-in view of the nodal B_θ field near $r = 0$ at times $t = 0.2$ and 0.8 μs, sampled at a location 2.5 mm above the midplane between the two electrode plates. There is no perceptible variation in the field along the length of the wire prior to initial expansion of the wire, so this sample is representative of the entire space between the plates at these early times. The data are extracted from the 3.8-element-per-wire-radius case (739,200 elements) for simulations using the R-Scaled and PSI-S formulations. At $t = 0.2$ μs, the expansion of the wire has not yet begun. At $t = 0.8$ μs, expansion is underway, and the field has started to distort, but the wire has not yet begun to burst.

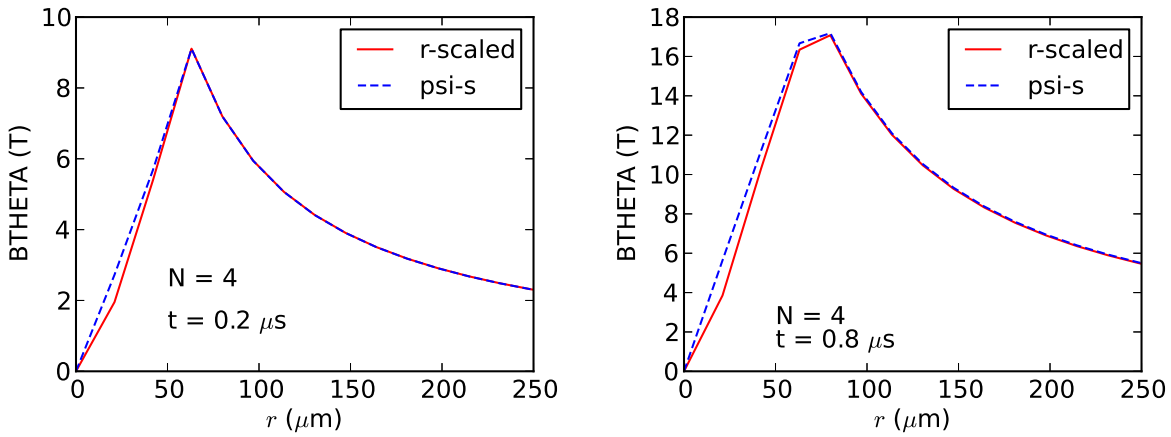

Figure 5.2: Radial profiles of B_θ at two times prior to burst for 2D exploding wire R-Scaled and PSI-S simulations at 3.8 elements per wire radius.

One can easily see the difference between the R-Scaled and the PSI-S formulations. The R-Scaled formulation has the deforming kink over the first few elements, while the PSI-S formulation

is accurately achieving the expected linear profile. This behavior should be anticipated, based on the results shown in Chapters 3 and 4. It suggests that the PSI-S formulation provides improved accuracy near the axis, which continues to affect the solution after motion of the wire has been initiated.

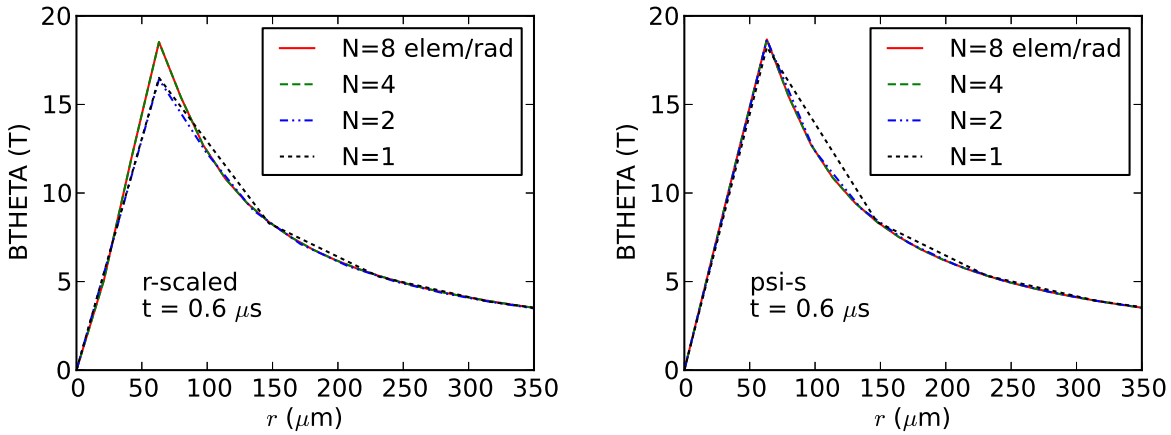

Figure 5.3: Radial profiles of B_θ at $t = 0.6$ μs for the 2D exploding wire simulations at various mesh resolutions for the R-Scaled and PSI-S formulations.

To demonstrate the dependence of the two formulations on the spatial resolution, we examine the same profiles, extracted from simulations at all four mesh resolution levels. This is shown in Figure 5.3. for both of the formulations, at $t = 0.6$ μs. This is prior to initiation of expansion in the wire near the midplane. At this early time, the profile of the B_θ field converges appropriately under mesh refinement. As expected, the solution for the PSI-S formulation degrades much more slowly as the mesh is coarsened, compared to the R-Scaled formulation. At N=2, the PSI-S result still nearly overlays the N=8 result, while the R-Scaled field deteriorates. Even at the very coarse N=1 level, the PSI-S result is acceptable. This suggests that the PSI-S formulation should allow MHD simulations to be run at lower resolution and thus lower cost for the user, without diminishing accuracy.

Evolution of Two-Dimensional Field Variables

Time evolution of the computed 2D density and current density fields during the explosion of the copper wire is shown for the two formulations in Figures 5.4 and 5.5, at 3.8 elements per wire radius. The orientation and magnitude of the enclosed current is depicted by plotting contours of the quantity $2\pi r B_\theta/\mu_0$. The images are zoomed in to the vicinity of the interface between the copper wire and the upper steel electrode plate. It is at these upper and lower interfaces where the explosion begins. Only very subtle deviations are apparent in the details of the solution at this stage of the solution between the two formulations, despite the noticeable differences seen in profiles of B_θ prior to burst. This suggests that the PSI-S formulation retains the desirable properties of the R-Scaled formulation for modeling the behavior of exploding wire systems, which have been

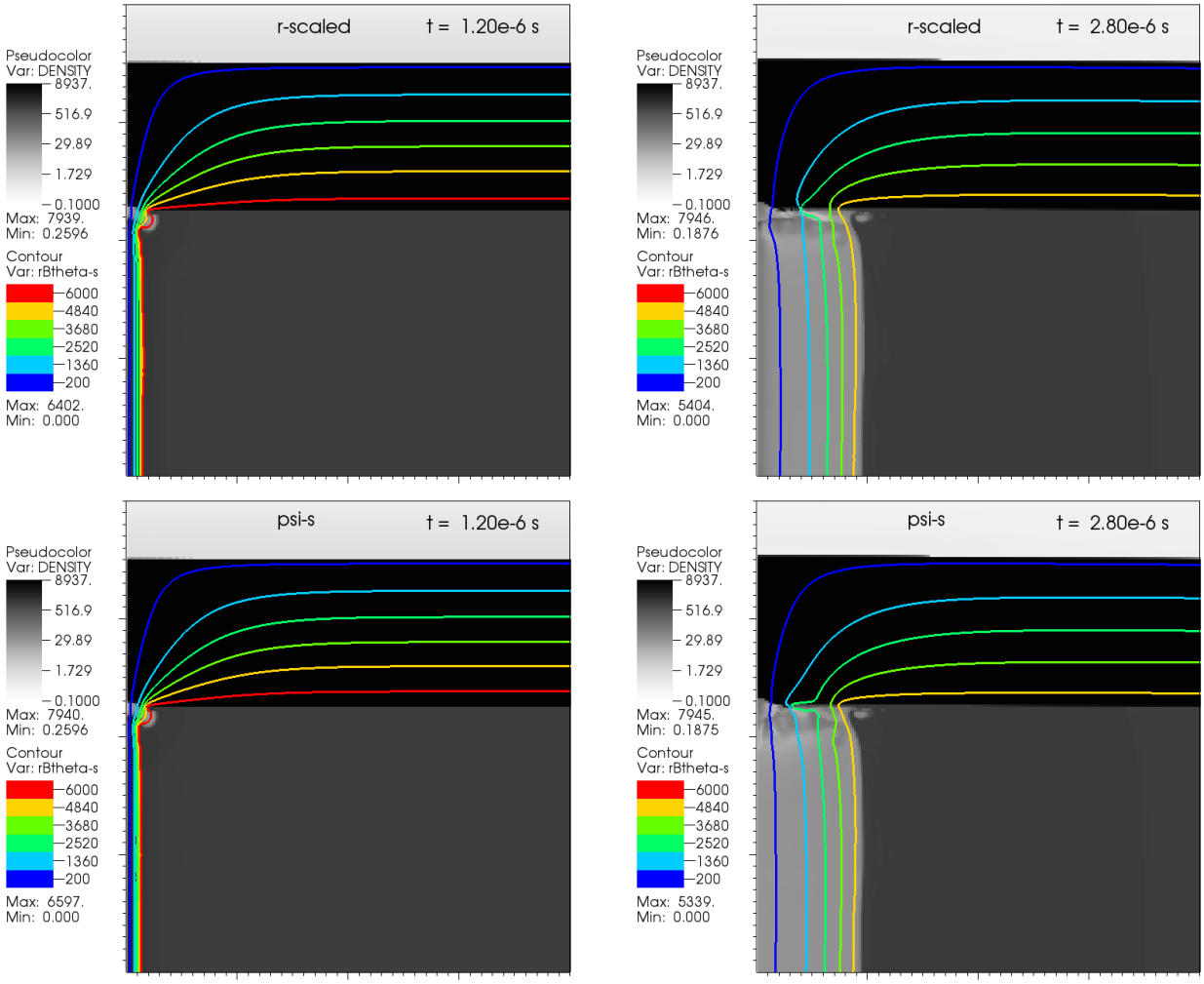

Figure 5.4: ALEGRA results for the exploding copper wire system, modeled using the r-scaled (top), and psi-s (bottom) representations at $N = 4$. The total density field is plotted, with contours of $2\pi r B_\theta/\mu_0$, at t = 1.2 and 2.8 μs.

demonstrated in previous work. [4] Meanwhile, it clearly improves the accuracy of the solution in the region near the axis.

In the solutions shown in Figures 5.4 and 5.5, the electrode experiences significant ablation as well as the wire. This environment of multimaterial ablation and extreme current densities places stringent requirements on the ALEGRA software, which must avoid prohibitively small timesteps and fatal conditions such as element inversion which can arise in these situations, particularly at N=4 and 8. The simulations here run successfully out to t=5 μs even at N=8, when ALEGRA's second-order "midpoint" time integration scheme is used, and an artificial viscosity scheme that includes hyperviscosity, coverage for both compression and expansion, and a Laplacian limiter to pinpoint shock fronts while excluding regions of smooth flow. The "multilevel" (ML) algebraic multigrid solver scheme for the iterative transient magnetics solve is also critical for running these simulations successfully in a massively parallel environment.

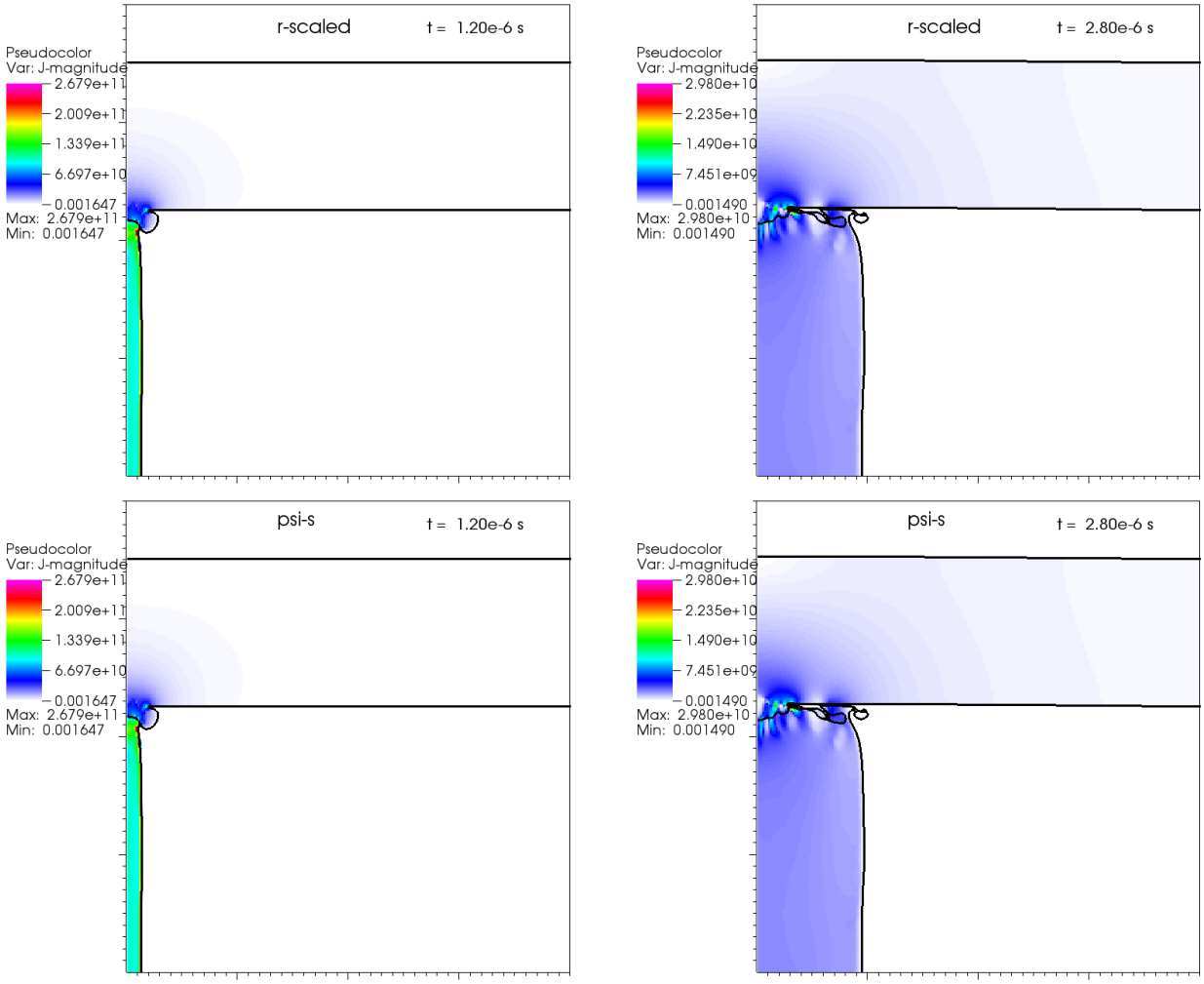

Figure 5.5: ALEGRA results for the exploding copper wire system, modeled using the r-scaled (top), and psi-s (bottom) representations at $N = 4$. The current density field is plotted, with overlaid material boundaries in black, at t = 1.2 and 2.8 μs.

Comparison to Experimental Circuit Data

The current and voltage characteristics of the exploding wire system provide a useful validation reference, and are compared here to ALEGRA simulations using the two formulations. In the experiments of Reference [2], the wires and circuit settings for the three tests were nominally identical, but uncertainties in dimensions and circuit parameters lead to variability in the results, as studied in References [4] and [5]. There was also some uncertainty in the timing of the capacitor discharge initiation, resulting from inherent "jitter" on the order of 100 ns in the function of the spark-gap switch used for initiation [14]. This provides a uncertain range within which the computed solutions should lie.

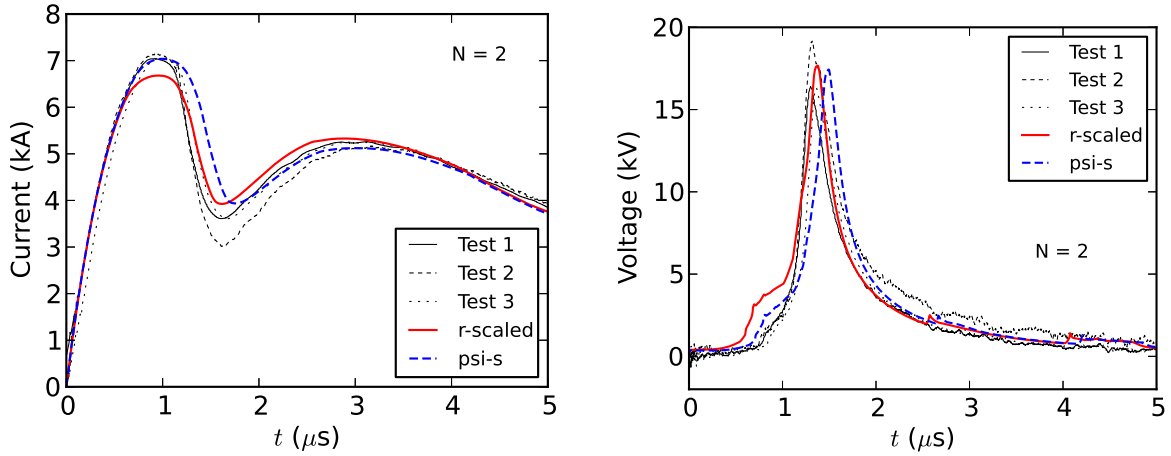

Figure 5.6: Time histories of current (left) and voltage (right) across the exploding wire, shown for the R-Scaled and PSI-S representations at 1.9 elements per wire radius, with comparison to measured data from three repeated experiments.

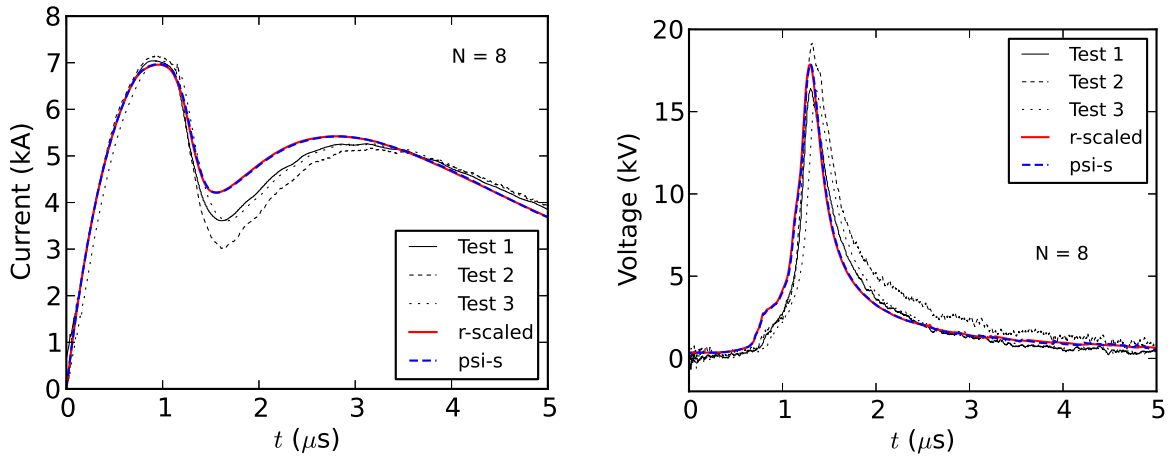

Figure 5.7: Time histories of current (left) and voltage (right) across the exploding wire, shown for the R-Scaled and PSI-S representations at 7.6 elements per wire radius, with comparison to measured data from three repeated experiments.

The experimental current and voltage histories are compared to the ALEGRA simulations on coarse and fine meshes (1.9 and 7.6 elements per wire radius) for the two formulations in Figures 5.6 and 5.7. We see that the prominent features of the circuit behavior are captured with good fidelity by the simulations using both formulations, on both the coarse and fine meshes. In particular, the time of peak voltage and peak current are captured with good accuracy, which is a very important aspect of these simulations, and is very sensitive to the details of the material model for the wire. The simulations also accurately capture the shape of the rising edge of the current pulse, indicating the magnetic field and associated self-inductance has been correctly computed.

Surprisingly, the improved PSI-S formulation has very little effect on the current and voltage

histories at high mesh resolution. Results from the two formulations nearly overlay each other in Figure 5.7. There is no visible difference in the time of peak voltage at this resolution. This is surprising because of the differences in current density and thermodynamic variables found in the transient-magnetics verification tests, discussed in Chapter 4. In the verification tests, the PSI-S formulation produces a larger rate of Joule heating because it correctly computes a uniform distribution of current density across the radius of the rod, while the R-Scaled formulation allows a signficant downward excursion to appear near the axis.

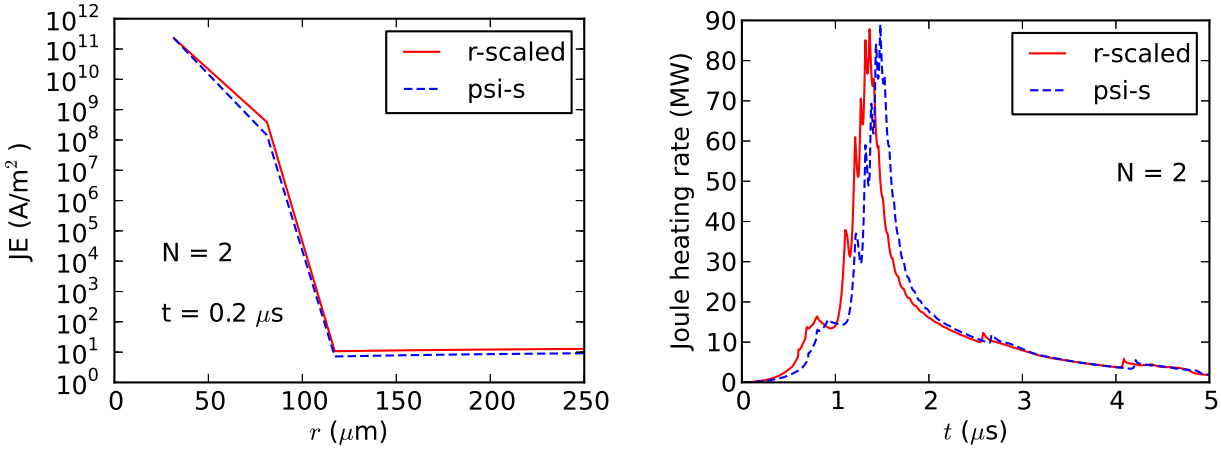

Figure 5.8: Left: radial profiles of current density at t=2 μs at 1.9 elements per wire radius. Right: time histories of the Joule heating rate at 1.9 elements per wire radius.

This effect does not occur in the exploding wire validation tests. As shown in the profiles of current density in Figure 5.8, the downward excursion in current density for R-Scaled does not appear. Further, the two formulations produce similar current density distributions, whose shape is also affected by the variable conductivity of the material and the transient nature of the magnetic diffusion process. Here, PSI-S in fact produces a slightly *lower* current density in some regions of the wire, which results in the slightly lower rate of Joule heating at these early times relative to the R-Scaled formulation, seen on the right-hand side of Figure 5.8. The effect is very small, even at coarse resolution, and vanishes as the mesh is refined. This effect is also responsible for the small difference in the "shoulder" region of the voltage history in Figure 5.6, at times between approximately 0.6 and 1.1 μs. This shoulder feature corresponds to phase transition in the wire material [4]. Here the PSI-S formulation is more faithful to the observed behavior. This leads to a much more accurate value of peak current for PSI-S than for the R-Scaled formulation at N=2. However, it also leads to a slightly later time of peak voltage, so some trade-off of effects is apparent.

Convergence of Wire Burst Timing

The timing of the burst event is a very important property of exploding wire systems, and one of the most important quantities of interest in these simulations. The time of wire burst is easily extracted from both experimental and simulation data by the voltage signature, which provides a characteristically prominent spike with a well-defined maximum. The time of this maximum voltage is often taken to be the burst time, which marks the approximate origin of the system of shock waves generated by the event.

The burst "action" is also an important property of these systems, characterizing in a general way the amount of energy deposition needed to achieve wire burst. In Reference [13], the specific action $g(t)$ is defined as

$$g(t) = \frac{1}{\pi a^2} \int_0^t I^2(t')dt' \tag{5.1}$$

where $I(t)$ is the current across the wire at time t, and a is the initial wire radius. The burst action g_b is the value of g at the time of wire burst t_b, which is the time of maximum voltage across the wire.

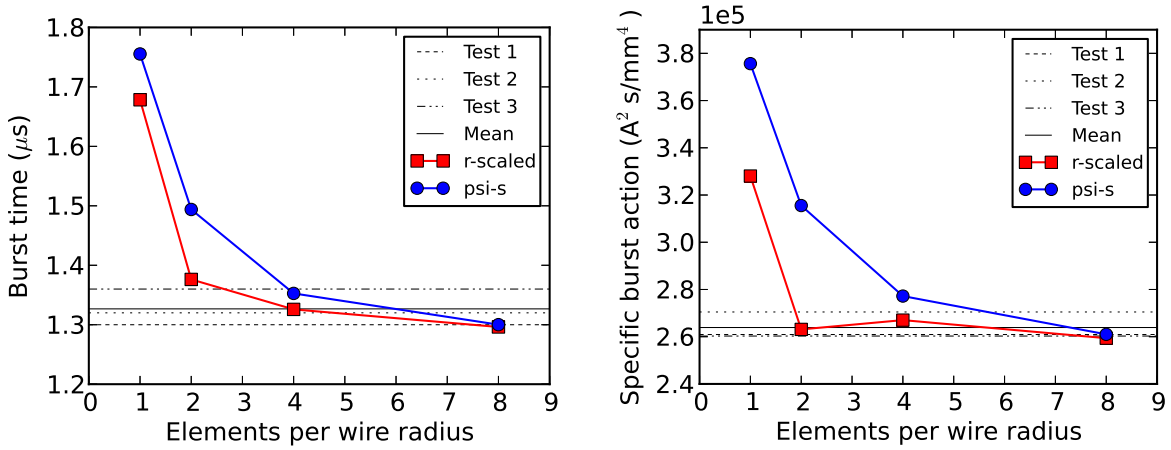

Figure 5.9: Burst time (left) and burst action (right) for experiments and simulations using R-Scaled and PSI-S representations at four mesh resolution levels.

This information can be conveniently requested as an output "response function" in the ALEGRA software, using the derived variable capability with time sampling. The burst time is captured using the "time of maximum value" and the burst action using the "at maximum of" commands. The final value of these response functions, which appear in ALEGRA output, then provides t_b and g_b.

The burst time and burst action trends with respect to mesh resolution are shown in Figure 5.9, with comparison to the experimental values. The ALEGRA simulations at high resolution

provide an excellent match to the experimentally measured values. At the highest resolution, the mean burst time and burst action from the experiments are both captured by the simulations to an accuracy of approximately 2%. At lower mesh resolution, the results quickly converge toward the reference values. Again surprisingly, the PSI-S results appear to converge at a slightly lower rate compared to the R-Scaled cases. Since the simulations all produce larger-than-realistic burst actions at low resolution, this difference is likely due to the slightly lower rate of Joule heating observed for PSI-S at early times. However, with PSI-S, the convergence trend for the burst action is completely monotonic, whereas for R-Scaled it oscillates slightly in the intermediate cases.

Tucker and Toth (1975) [13] developed a simple circuit analysis code to calculate burst action and burst energy values for many different metals, which they matched to empirical data. Their value for copper was $g_b = 1.73 \times 10^5$ A^2s/mm^4. Experimental values extracted for this study average to 2.64×10^5 A^2s/mm^4. The simulation values at $N = 8$ are 2.59×10^5 and 2.61×10^5 A^2s/mm^4, respectively, for R-Scaled and PSI-S. These values differ by about 50% from Tucker and Toth's reference value, but they cautioned that their analysis was invalid for current densities larger than 10^{11} A/m^2, which is near the largest values attained in these simulations.

Computational Performance Data

The runtime data for these simulations provides further information as to the usefulness of the PSI-S formulation. Total CPU time for each of the eight tests is recorded in Table 5.1, along with some other details of the simulation. Here it is apparent that for these tests the two formulations have roughly equivalent performance, except at the highest resolution. At 7.6 elements per wire radius, the PSI-S simulation runs to completion 40% faster than the R-Scaled formulation.

Table 5.1: Runtime statistics for exploding wire simulations.

Case	Total CPU (s) R-Scaled	Total CPU (s) PSI-S	Element count	Cores	Elements per core
N=1	6.65e+2	6.82e+2	45,900	16	2869
N=2	3.96e+3	3.62e+3	184,200	32	5756
N=3	6.87e+3	6.77e+3	739,200	80	9240
N=3	5.97e+4	3.93e+4	2,959,200	320	9247

Further analysis shows that this is due to the higher rate of Joule energy deposition with the R-Scaled formulation, which results in higher material temperatures, particularly at high resolution. The copper and steel temperatures are limited to 50,000 K, but the water in the gap has no limits, and at high resolutions its temperature becomes extremely high in some locations at high resolution with the R-Scaled formulation, resulting in a relatively low (but not fatally low) timestep. This is responsible for the larger runtimes. We conclude that, overall, the cost of using PSI-S compared to R-Scaled is equivalent or lower.

Chapter 6

Conclusion

We sought to implement a new formulation of the two-dimensional cylindrical symmetric magnetic diffusion equation using a coordinate transformation inspired by Melissen and Simkin[10]. We explained the transformation and used it to derive a new equation set and the finite element counterparts and implemented this capability in ALEGRA. We then performed a verification analysis to show the superiority of the new PSI-S formulation over the previously implemented FIFE and R-Scaled formulations. For our verification study, we used a wire in a void model in axisymmetric geometry with a constant, axial-tangential electric field assumed to be on the interface of the rod and the void, for which we were able to find an analytic solution using Laplace transform techniques and perturbation theory. Due to the perturbation solution being non-uniformly accurate near $t = 0$, it was unsatisfactory for completing our verification study. We manufactured a new solution fully compatible with our time dependent solution in the rod, and used it to successfully complete our verification analysis. In the process we gave detailed and convincing evidence of the impracticality of the FIFE formulation for large axisymmetric application problems with material conductivity jumps and changes.

Thereafter, we showed some additional benefits of the PSI-S formulation via demonstration of more accurate computations of the temperature, pressure, and current density variables. We also discussed a simple verification test for the radial current density formula.

We additionally carried out a validation study using the PSI-S and R-Scaled formulations to simulate the exploding copper wire experiments of DeSilva and Vunni [2]. Disparities between solutions using these two methods were very subtle for these simulations. For both formulations, the prominent features of the experimental current and voltage histories were captured with very good accuracy, including the time of peak current and voltage, and the current rise rate. The simulations also generally showed monotonic convergence under spatial refinement, and burst time and burst action were both captured within an accuracy of a few percent relative to the experimental data.

Some details were represented more faithfully by the PSI-S formulation, particularly at early times when most of the current flows near the axis. Other details were captured better using the R-Scaled formulation. However, in both cases the differences were very subtle, and confined to coarse meshes. We can conclude that the PSI-S formulation preserves the desirable properties of the R-Scaled formulation (which was used for the analyses appearing in References [4] and [5], while improving substantially the accuracy of the representation near the axis.

In our analysis we have shown how verification studies can be particularly sensitive to the accuracy and precision of the analytic solution used. However, we also proposed and utilized a fairly general technique for easily manufacturing physically interesting analytic solutions using classical separation-of-variable methods which allows for construction of interesting analytic solutions with material property jumps given a solution for uniform properties in one region.

The PSI-S formulation is now coded into ALEGRA and ready for use and distribution. It has yet to be determined whether the PSI-S formulation is reliable enough to become the default axisymmetric magnetic diffusion formulation. However, we believe that we have now made a very strong case for adopting this feature for production use.

Appendix A

A_z by Inverse Laplace Transform and Residue Theory

Applying the inverse Laplace transform to $\hat{A}_z$ gives

$$A_z = \frac{1}{2\pi i}\int_B e^{ut}\frac{-V}{hu^2}\left(\frac{I_0(\sqrt{\mu_0\sigma_r u}r)}{I_0(\sqrt{\mu_0\sigma_r u}a)}-1\right)du \tag{A.1}$$

where B is the Bromwich contour. The setup is perfect for an application of the residue theorem, so we consider the poles of the function within the integral. The poles are at $u=0$ and the roots of $I_0(\sqrt{\mu_0\sigma_r u}a)$. Because we can effectively deal with all the roots of the I_0 term at once, we first address $u=0$, and then we address $I_0(\sqrt{\mu_0\sigma_r u}a)=0$.

u = 0

Let γ be a closed contour around $u=0$ does not enclose any value of u such that $I_0(\sqrt{\mu_0\sigma_r u}a)=0$, then

$$\frac{1}{2\pi i}\int_\gamma e^{ut}\frac{-V}{hu^2}\left(\frac{I_0(\sqrt{\mu_0\sigma_r u}r)}{I_0(\sqrt{\mu_0\sigma_r u}a)}-1\right)du = \frac{1}{2\pi i}\int_\gamma f(u)du = \mathrm{Res}(f,0) \tag{A.2}$$

Note that

$$I_0(x) = \sum_{m=0}^{\infty}\frac{1}{m!\Gamma(m+1)}\left(\frac{x}{2}\right)^{2m} = \sum_{m=0}^{\infty}\frac{1}{2m!}\left(\frac{x^2}{4}\right)^m \tag{A.3}$$

therefore, we can find $\text{Res}(f,0)$ by expanding I_0 in $f(u)$.

$$
\begin{aligned}
f(u) &= e^{ut}\left(-\frac{V}{hu^2}\right)\left(\frac{I_0(\sqrt{\mu_0\sigma_r u}r) - I_0(\sqrt{\mu_0\sigma_r u}a)}{I_0(\sqrt{\mu_0\sigma_r u}a)}\right) \\
&= e^{ut}\left(-\frac{V}{hu^2}\right)\left(\frac{\sum_{m=0}^{\infty}\frac{1}{2m!}\left(\frac{\mu_0\sigma_r u r^2}{4}\right)^m - \sum_{m=0}^{\infty}\frac{1}{2m!}\left(\frac{\mu_0\sigma_r u a^2}{4}\right)^m}{\sum_{m=0}^{\infty}\frac{1}{2m!}\left(\frac{\mu_0\sigma_r u a^2}{4}\right)^m}\right) \\
&= e^{ut}\left(-\frac{V}{hu^2}\right)\left(\frac{\sum_{m=0}^{\infty}\frac{1}{2m!}\left(\frac{\mu_0\sigma_r u}{4}\right)^m (r^{2m}-a^{2m})}{\sum_{m=0}^{\infty}\frac{1}{2m!}\left(\frac{\mu_0\sigma_r u a^2}{4}\right)^m}\right) \\
&= e^{ut}\left(-\frac{V}{hu^2}\right)\left(\frac{1+\frac{\mu_0\sigma_r u}{4}(r^2-a^2)+\frac{1}{4}\left(\frac{\mu_0\sigma_r u}{4}\right)^2(r^4-a^4)+\cdots}{1+\left(\frac{\mu_0\sigma_r u a^2}{4}\right)+\frac{1}{4}\left(\frac{\mu_0\sigma_r u a^2}{4}\right)^2+\cdots}\right) \\
&= e^{ut}\left(-\frac{V}{h}\right)\left(\frac{1+\frac{\mu_0\sigma_r}{4u}(r^2-a^2)+\frac{1}{4}\left(\frac{\mu_0\sigma_r}{4}\right)^2(r^4-a^4)+\cdots}{1+\left(\frac{\mu_0\sigma_r u a^2}{4}\right)+\frac{1}{4}\left(\frac{\mu_0\sigma_r u a^2}{4}\right)^2+\cdots}\right) \qquad \text{(A.4)}
\end{aligned}
$$

The u^{-1} term is corresponds to the Residue, so

$$\text{Res}(f,0) = -\frac{\mu_0\sigma_r V}{4h}(r^2-a^2) \qquad \text{(A.5)}$$

Roots of I_0

We now redefine our Bromwich contour to not contain $u=0$, but still contain all other poles of $I_0(\sqrt{\mu_0\sigma_r u}a)$, which are all on the negative x-axis. Our methodology for this case is to rewrite our function f in terms of two holomorphic functions h and g, such that $f=\frac{g}{h}$, then $\text{Res}(f,c)=\frac{g(c)}{h'(c)}$ for each pole c. Before we start, however, we point out a few identities we will use later on:

- $I_0(x) = J_0(ix)$, where J_0 is the zero order Bessel function of the first kind
- $I_0'(x) = iJ_0'(ix)$
- $J_0(-x) = J_0(x)$

- $J_0'(-x) = -J_0'(x)$

Let

$$g(u) = e^{ut}\left(-\frac{V}{hu^2}\right)\left(I_0(\sqrt{\mu_0\sigma_r u}r) - I_0(\sqrt{\mu_0\sigma_r u}a)\right) \tag{A.6}$$

$$h(u) = I_0(\sqrt{\mu_0\sigma_r u}a) \tag{A.7}$$

and

$$\alpha_n = -\frac{k_n^2}{\mu_0\sigma_r a^2}. \tag{A.8}$$

Then, $g(\alpha_n) \neq 0$ as long as $r \neq a$ and $h(\alpha_n) = I_0(ik_n) = J_0(-k_n) = J_0(k_n) = 0$. Now,

$$h'(u) = \frac{a}{2}\sqrt{\frac{\mu_0\sigma_r}{u}}I_0'(\sqrt{\mu_0\sigma_r u}a)$$

so

$$h'(\alpha_n) = \frac{\mu_0\sigma_r a^2}{2}\sqrt{\frac{1}{-k_n^2}}I_0'(\sqrt{-k_n^2})$$

$$= \frac{\mu_0\sigma_r a^2}{2}\frac{1}{ik_n}I_0'(ik_n)$$

$$= \frac{\mu_0\sigma_r a^2}{2}\frac{1}{ik_n}iJ_0'(i^2k_n)$$

$$= \frac{\mu_0\sigma_r a^2}{2}\frac{1}{k_n}J_0'(-k_n)$$

$$= -\frac{\mu_0\sigma_r a^2}{2}\frac{1}{k_n}J_0'(k_n)$$

$$\neq 0$$

Thus the residue theorem holds, and we may compute the remaining integral.

$$\frac{1}{2\pi i}\int_{B'} f(u)du = \sum_n Res(f,\alpha_n)$$

$$= \sum_{n=1}^{\infty}\left(\frac{g(\alpha_n)}{h'(\alpha_n)}\right)$$

$$= \sum_{n=1}^{\infty}\frac{e^{\frac{-k_n^2 t}{\mu_0\sigma_r a^2}}\left(-\frac{\mu_0^2\sigma_r^2 a^4 V}{hk_n^4}\right)\left(I_0(\frac{ik_n r}{a})-I_0(ik_n)\right)}{-\frac{\mu_0\sigma_r a^2}{2}\frac{1}{k_n}J_0'(k_n)}$$

$$= \sum_{n=1}^{\infty}\frac{e^{\frac{-k_n^2 t}{\mu_0\sigma_r a^2}}\left(\frac{2\mu_0\sigma_r a^2 V}{hk_n^3}\right)\left(J_0(\frac{k_n r}{a})-J_0(k_n)\right)}{J_0'(k_n)}$$

$$= \frac{2\mu_0\sigma_r a^2 V}{h}\sum_{n=1}^{\infty}\frac{e^{\frac{-k_n^2 t}{\mu_0\sigma_r a^2}}J_0(\frac{k_n r}{a})}{k_n^3 J_0'(k_n)} \tag{A.9}$$

The total value of the integral is sum of the residues, so our final result is:

$$A_z = \frac{1}{2\pi i}\int_B f(u)du$$

$$= -\frac{\mu_0\sigma_r V}{4h}(r^2-a^2) + \frac{2\mu_0\sigma_r a^2 V}{h}\sum_{n=1}^{\infty}\frac{e^{\frac{-k_n^2 t}{\mu_0\sigma_r a^2}}J_0(\frac{k_n r}{a})}{k_n^3 J_0'(k_n)}$$

$$= \frac{-\mu_0\sigma_r V}{h}\left(\frac{(r^2-a^2)}{4} - 2a^2\sum_{n=1}^{\infty}\frac{e^{\frac{-k_n^2 t}{\mu_0\sigma_r a^2}}J_0(\frac{k_n r}{a})}{k_n^3 J_0'(k_n)}\right) \tag{A.10}$$

Appendix B

FIFE convergence

The results for the FIFE formulation driven with electric field boundary conditions at $t = 1.5\mu s$ with 100-3200 elements shows that the method is formally correct but vastly less optimal for practical purposes when compared with results for the PSI-S formulation given in the text. In particular, note that in the manufactured solution case, mesh resolutions of around 1000 elements are required to start seeing second order accuracy in both the rod and the void.

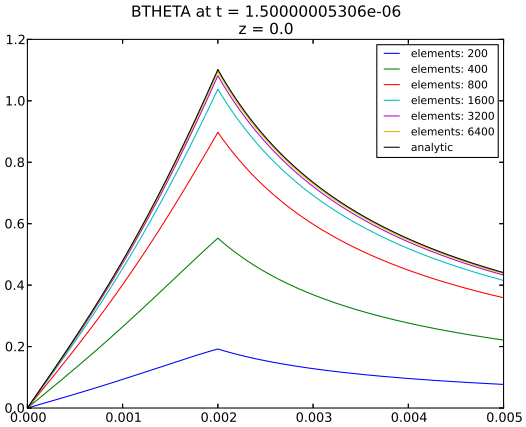

Number of elements per block	Order of convergence
100	7.46302e-01
200	7.46302e-01
400	1.42963e+00
800	1.67216e+00
1600	1.63780e+00
3200	1.49193e+00

Figure B.1: Perturbation Solution

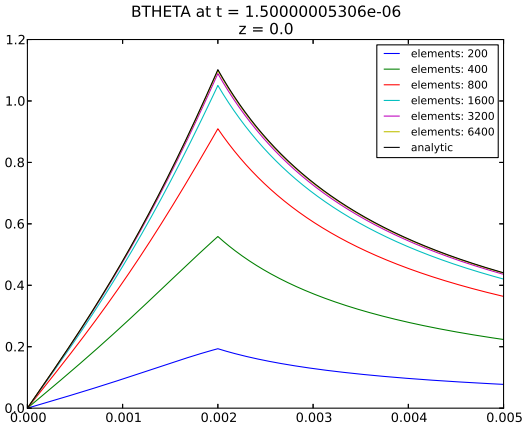

Number of elements per block	Order of convergence
100	7.60723e-01
200	7.60723e-01
400	1.50851e+00
800	1.91023e+00
1600	2.01595e+00
3200	2.00151e+00

Figure B.2: Manufactured Solution

References

[1] W. G. Chace. *A Brief Survey of Exploding Wire Research*. Plenum Press, 1959.

[2] A. W. DeSilva and G. B. Vunni. Electrical conductivity of dense Al, Ti, Fe, Ni, Cu, Mo, Ta, and W plasmas. *Phys. Rev. E*, 83(037402), 2011.

[3] M. P. Desjarlais. Practical improvements to the Lee-More conductivity near the metal-insulator transition. *Contrib. Plasma Phys.*, 41(2-3):267–270, 2008.

[4] R. Doney, G. Vunni, and J. Niederhaus. Experiments and simulations of exploding aluminum wires: validation of ALEGRA-MHD. Technical Report ARL-TR-5299, Army Research Laboratory, Aberdeen Proving Ground, MD, 2010.

[5] R. R. Drake, J. H. J. Niederhaus, and D. R. Koenig. A parametric study in MHD modeling for exploding wires using DAKOTA in ALEGRA. Aberdeen Proving Grounds, MD, May 2012. Proceedings of the Army Research Laboratory Reseach in Ballistic Protection Technologies Workshop. https://cfwebprod.sandia.gov/cfdocs/CompResearch/docs/ExplodingWireUUR_paper.pdf.

[6] A. C. Robinson et al. Alegra: An arbitrary Lagrangian-Eulerian multimaterial, multiphysics code. Reno, Nevada, January 2008. Proceedings of the 46th AIAA Aerospace Sciences Meeting. AIAA-2008-1235.

[7] A. Grinenko, S. Efimov, A. Fedotov, and Ya. E. Krasik. Efficiency of the shock wave generation caused by underwater electrical wire explosion. *J. Appl. Phys.*, 100(113509), 2006.

[8] T. A. Haill and A. C. Robinson. Two-Dimensional Finite-Element Magnetohydrodynamic Equations in ALEGRA, Part I: Magnetic Field Formulation. Technical report, SNL, working draft.

[9] P. Knupp and K. Salari. *Verification of Computer Codes in Computational Science and Engineering*. Chapman and Hall/CRC, 2002.

[10] J.B.M. Melissen and J. Simkin. A New Coordinate Transform for the Finite Element Solution of Axisymmetric Problems in Magnetostatics. *IEEE Transactions on Magnetics*, 26(2):391–394, March 1990.

[11] P. O'Malley and C. J. Garasi. Understanding the electrical interplay between a capacitive discharge circuit and exploding metal. Technical Report SAND2015-1132, Sandia National Laboratories, Albuquerque, NM, February 2015.

[12] G. S. Sarkisov, S. E. Rosenthal, K. R. Cochrane, K. W. Struve, C. Deeney, and D. H. McDaniel. Nanosecond electrical explosion of thin aluminum wires in a vacuum: experimental and computational investigations. *Phys. Rev. E*, 71(046404), 2005.

[13] T. J. Tucker and R. P. Toth. EBW1: a computer code for the prediction of the behavior of electrical circuits containing exploding wire elements. Technical Report SAND75-0041, Sandia National Laboratories, Albuquerque, NM, February 1975.

[14] G. B. Vunni. private communication, June 2014.

Distribution

External Distribution:

U.S. Army Research Laboratory
Attn:
Robert L. Doney (electronic copy)
Misha Grinfeld (electronic copy)
George Vunni (electronic copy)
James Cazamias (electronic copy)

Lawrence Livermore National Laboratory
Attn:
Thomas A. Brunner, (electronic copy)
Joseph M. Koning, (electronic copy)

Los Alamos National Laboratory
Attn:
Christopher L. Rousculp (electronic copy)

Internal Distribution:

Bryan V. Oliver, 01340 (electronic copy)
Leonard Lorence, 01341 (electronic copy)
John N. Shadid, 01442 (electronic copy)
Eric C. Cyr, 01442 (electronic copy)
Glen Hansen, 01443 (electronic copy)
Richard M. J. Kramer, 01443 (electronic copy)
Sharon Petney, 01443 (electronic copy)
Allen C. Robinson, 01443 (electronic copy)
Christopher Siefert, 01443 (electronic copy)
Martin W. Heinstein, 01542 (electronic copy)
James M. Reynolds, 01555 (electronic copy)
John Niederhaus, 01446 (electronic copy)
William J. Rider, 01446 (electronic copy)
Kyle Cochrane, 01641 (electronic copy)
Thomas A. Haill, 01641 (electronic copy)
Raymond W. Lemke, 01641 (electronic copy)
Thomas A. Gardiner 01641 (electronic copy)
Heath L. Hanshaw 01641 (electronic copy)

Matthew M. Martin 01641 (electronic copy)
Thomas A. Mattsson, 01641 (electronic copy)
Andrew J. Porwitzky 01641 (electronic copy)
Jean-Paul Davis 01646 (electronic copy)
Mark Hess, 01684 (electronic copy)
Kyle Peterson, 01684 (electronic copy)
Matthew R. Weis, 01684 (electronic copy)
Edmund Yu, 01684 (electronic copy)
Christopher J. Garasi, 02552 (electronic copy)

Technical Library, 09536 (electronic copy)

Sandia National Laboratories